Post-print version of the paper by Lu et al.
in Int J Cold Region of Science and Technology, 156 (2018) 102-116,
https://doi.org/10.1016/j.coldregions.2018.07.011

Parallel Channels' Fracturing Mechanism during Ice Management Operations. Part II: Experiment

Wenjun Lu[1] **Raed Lubbad** **Sveinung Løset**

Sustainable Arctic Marine and Coastal Technology (SAMCoT), Centre for Research-based Innovation (CRI)

Norwegian University of Science and Technology (NTNU), Trondheim, Norway

(To be submitted to <Cold Regions Science & Technology> special issue)

[1] Corresponding author
E-mail address: wenjun.lu@ntnu.no (Wenjun Lu)

Post-print version of the paper by Lu et al.
in Int J Cold Region of Science and Technology, 156 (2018) 102-116,
https://doi.org/10.1016/j.coldregions.2018.07.011

Contents

Post-print version of the paper by Lu et al.
in Int J Cold Region of Science and Technology, 156 (2018) 102-116,
https://doi.org/10.1016/j.coldregions.2018.07.011

Post-print version of the paper by Lu et al.
in Int J Cold Region of Science and Technology, 156 (2018) 102-116,
https://doi.org/10.1016/j.coldregions.2018.07.011

Abstract

During ice management operations, cutting parallel channels with narrow spacing in the ice using icebreakers can effectively reduce the size of ice floes reaching the protected vessel/structure. A narrow channel spacing width generates smaller ice floes. However, a spacing that is too narrow can lead to excessive or even impractical ice management operations. Therefore, it is beneficial to establish a theoretical model that correlates the channel spacing width with the frequency of ice fracturing events and the reduction of managed ice floe sizes. This is achieved in the current study with two sequential papers, i.e. Papers I and II. In Paper I, a theoretical model involving an 'edge crack model' was formulated to predict the following conditions for an ice management operation: 1) the maximum ice floe with size L_{MCD} that can be produced; 2) the maximum channel spacing width $h_{\max}$ beyond which long cracks will not develop between the channels; and 3) the required force to initiate long cracks between parallel channels. In this paper (Paper II), we describe two dedicated 'parallel channel tests' conducted separately on September 26th and 29th in 2015 during an expedition to the Arctic Ocean (around 82° N and 16° E) with the icebreakers Oden and Frej. The tests had 'well-controlled' channel spacing in each test run. Several different channel spacing values were tested with the Oden and the consequent fracturing information was documented by camera images. Image processing enabled us to extract information, such as maximum floe sizes and floe size distributions, given different channel spacing widths. In addition, the ship's data, such as ship velocity and propulsion history, enabled us to validate the theoretical model's capability to predict the onset of long cracks between two parallel channels. Despite uncertainties (e.g., non-uniform ice thickness, fracture properties of sea ice, etc.) involved in the tests, favourable comparisons between the experimental results and the theoretical predictions were achieved. Both the theoretical model and experimental results help clarify the parallel channel fracturing mechanism.

Keywords:

Ice management operations; Parallel channels; Ship–ice interactions; Image Processing; Multi-body Dynamics;

Post-print version of the paper by Lu et al.
in Int J Cold Region of Science and Technology, 156 (2018) 102-116,
https://doi.org/10.1016/j.coldregions.2018.07.011

1 Introduction

One of the primary goals for icebreakers during an ice management operation is to break the incoming ice features with maximal efficiency. In this regard, fracturing sea ice plays an important role. In principle, one may increase the number of icebreakers or employ more powerful and versatile ones to increase the overall fracturing efficiency. Tactically, one must consider the given icebreaking resources to design an optimal icebreaking pattern that incorporates the varying environmental factors, e.g., ice drifting speed, directional variation and ice properties, such that 1) the ice floe size reduction is under the design threshold; and 2) the protected asset is within the created channel. Practically, for effective and uniform downstream floe size reduction, the deployed icebreakers are expected to follow a systematic track pattern and tackle all ice floes that are encountered, no matter the size (Hamilton et al., 2011a). Depending on ice drifting speeds, directional variations, and ice properties, the optimal shape of the icebreaker's track pattern varies. Despite this variety, most of the track patterns create successive 'parallel' channels in the ice field. In between two successive parallel channels, long cracks usually form and effectively lead to floe size reductions.

This parallel channel fracturing phenomenon is important to consider while planning the deployment of a fleet of icebreakers for an ice management operation. It directly influences the produced ice floe sizes downstream of the icebreakers. For example, Hamilton et al. (2011a, 2011b) developed a numerical simulator to quantify the effectiveness of an ice management operation (e.g., downstream floe size distribution). Within the simulator, the outgoing floe size was assumed to be equivalent to the spacing between two successive parallel channels (i.e., produced floe size L : Channel spacing h $\approx$1:1). Similar floe size distributions were also observed in other ice management trials (Farid et al., 2014, Lubbad et al., 2012, Lubbad et al., 2013). However, to the authors' knowledge, until now, there are no existing theoretical formulations with well-controlled tests in relation to the parallel channel fracturing mechanisms that are reported in the literature.

Therefore, in a series of two papers, we strive to offer both a theoretical explanation (Paper I) and experimental validation (Paper II) of the observed parallel channel fracturing mechanism. In Paper I, a theoretical model concerning an edge crack's propagation was proposed and formulated to predict 1) the maximum channel spacing $h_{\max}$ beyond which long cracks cease to develop; and 2) the maximum ice floe size L_{MCD} that can be generated between two parallel channels. In this paper (i.e., Paper II), we report two dedicated field tests during the Oden Arctic Technology Research Cruise in 2015 (OATRC2015) in the Arctic Ocean (Lubbad et al., 2016). With the icebreaker Oden, the first parallel channel test was carried out on September 26th from 13:00 to 14:00 (unless

Post-print version of the paper by Lu et al.
in Int J Cold Region of Science and Technology, 156 (2018) 102-116,
https://doi.org/10.1016/j.coldregions.2018.07.011

otherwise stated, UTC time is used in this paper). Valuable information from helicopter images was collected during this first test. The second parallel channel test was conducted on September 29th from 08:00 to 11:30, which showed well-controlled channel spacing. During the second test, cracks propagating between two successive parallel channels were documented by a dedicated on-board camera. This paper focuses on the test description, data interpretation, comparison with proposed theoretical models, and fracture mechanism discussion.

2 Background

Before we proceed to the detailed test descriptions, it is beneficial to provide a brief description of the theoretical development carried out in Paper I to reveal the important parameters that are to be measured for validation purposes. To explain the mechanism of long crack formation, Paper I presented a theoretical model regarding the ship–ice interaction with the presence of a neighbouring free channel. This model is re-sketched in Fig. 1, with Oden as an example. Fig. 1a illustrates the major parameters utilised in the proposed interaction model. Fig. 1b illustrates the force components F_X and F_Y that are applied on the ice sheet through contact with the ship's bow. The influence from both force components are considered in the proposed theoretical model.

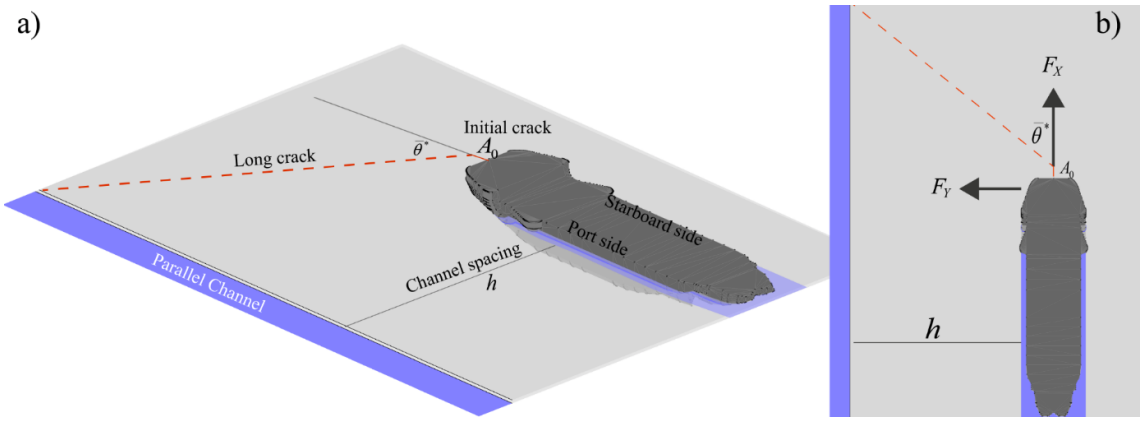

Fig. 1. Interaction model proposed for the parallel channels' fracture mechanism, with Oden as an example, a) perspective view with major geometric definitions; b) top view with the force components applied to the ice sheet.

Following the interaction model in Fig. 1, two groups of equations were developed. The first group of equations is re-written in Eq. (1), in which the relationship between the channel spacing h and the contact forces F_X and F_Y are established by an 'edge crack model' (detailed information can be found in Paper I).

Post-print version of the paper by Lu et al.
in Int J Cold Region of Science and Technology, 156 (2018) 102-116,
https://doi.org/10.1016/j.coldregions.2018.07.011

$$
\begin{aligned}
&h = (\frac{F_X}{tK_{IC}})^2[f_1^2(\frac{A_0}{h},\beta_{YX}) + f_2^2(\frac{A_0}{h},\beta_{YX})] \\
&\beta_{YX} = \frac{F_Y}{F_X} \\
&f_1(\frac{A_0}{h},\beta_{YX}) = \sqrt{\frac{4\pi}{\pi^2-4}}(\frac{A_0}{h})^{-1/2}(\beta_{YX}-\frac{1}{\pi}) + \frac{2.0284(A_0/h)+2.9890}{(A_0/h)^{1.3569}+1.0499}\beta_{YX} + \frac{1}{2}\frac{0.1856\text{-}0.2174(A_0/h)^{0.1635}}{(A_0/h)^{6.2861}+0.4092(A_0/h)^{0.1635}} \\
&f_2(\frac{A_0}{h},\beta_{YX}) = \frac{1.8134(A_0/h)+0.5498}{(A_0/h)^{1.4702}+1.2041}\beta_{YX} + \frac{1}{2}\frac{0.4051-1.3238(A_0/h)^{0.4339}}{(A_0/h)^{0.9953}+1.0099(A_0/h)^{0.4339}}
\end{aligned}
\tag{1}
$$

In Eq. (1),

t is the ice thickness [m];

A_0 is the initial crack length, which can be approximated by $A_0 = 2\ell$;

$\ell = \sqrt[4]{D/k}$ is the characteristic length expressed by the flexural rigidity $D = Et^3/[12(1-\nu^2)]$ and fluid foundation stiffness $k = \rho_w g$ (with more details presented in Paper I);

K_{IC} is the fracture toughness of sea ice [kPa$\sqrt{\text{m}}$];

$f_i(\frac{A_0}{h},\beta_{YX})$ are functions dependent on the ratio of A_0/h and the interaction force ratio β_{YX}; they were fitted from numerical simulations together with theoretical asymptotic analysis.

Eq. (1) quantifies the minimum force F_X that is required to propagate the existing crack that may eventually lead to a long crack between the parallel channels with spacing h. Therefore, in the designed tests, it is important to measure/control the channel spacing, document the occurrences/absence of long cracks, and provide an account of the available contact force F_X.

The second group of equations characterises the parallel channels' fracturing path in a simplified fashion with an easy-to-implement numerical recipe presented in Paper I (Table 1), to identify an intermediate variable $L'_{\max}$, which is derived further to the variable $L_{\max}$ and maximum floe size L_{MCD} according to Eq. (2), as follows:

$$
\begin{aligned}
&L_{\max} = f_3(P/Q)\cdot L'_{\max} \\
&f_3(P/Q) = 0.0334P/Q + 1.1813 \\
&L_{MCD} = \sqrt{4(L_{\max}h)/\pi}
\end{aligned}
\tag{2}
$$

in which, $L'_{\max}$ is calculated with the numerical recipe in Table 1 of Paper I, taking into account the idealised crack tip's Stress Intensity Factors (SIFs), which further determines the crack's kink angle; $f_3(P/Q)$ is function obtained by fitting the numerical results to scale $L'_{\max}$ up; L_{MCD} is derived following the conventional definition

Post-print version of the paper by Lu et al.
in Int J Cold Region of Science and Technology, 156 (2018) 102-116,
https://doi.org/10.1016/j.coldregions.2018.07.011

of a Mean Calliper Diameter (MCD) of an ice floe. It represents the diameter of a disk which has the same area of a geometry of irregular shape.

A further exploitation of Eq. (2) leads to the formulation of the maximum floe size ratio between two parallel channels, as shown in Eq. (3).

$$\text{Maximum floe ratio} = L_{MCD} / h = \sqrt{4(L_{\max} / h) / \pi} \tag{3}$$

To verify Eqs. (2) and (3), the paths of the developed long cracks and floe size ratio between the parallel channels should be documented in the tests. This is achieved via the different camera systems that were employed in the tests.

3 Test Description

Bearing in mind the relationships among the important parameters stated above, we carried out 'parallel channel tests' during OATRC2015. Two icebreakers (Oden and Frej) were employed during the research cruise in the Arctic Ocean (around 82° N and 16 ° E). Both icebreakers are heavily instrumented for various research activities (Lubbad et al., 2016). Performing the ice management trials using a range of supporting hardware and software were among the prioritised activities (Shafrova et al., 2016, Hamilton et al., 2016, Matskevitch et al., 2016). Because most ice management operations involve the creation of parallel channels, we were privileged with an abundant amount of data for the evaluation of their fracturing mechanisms. In particular, among all these ice management operations, two dedicated 'parallel channel tests' were carried out by the icebreaker Oden with strictly controlled channel spacing h and a continuous logging of ship data (i.e., ship's position, inertia, propulsion and wind data).

3.1 Channel Spacing and Ship Data

During the test, the channel spacing h was measured by a laser rangefinder with an accuracy to meters; and was maintained by the captain to his best capability. Even though the spacing was prescribed as a constant value while planning the tests, it is rather challenging to maintain an accurate and consistent channel spacing due to practical limits imposed by varying ice drifting speeds and directions and inhomogeneous ice features. During the tests, the actual channel spacing values were logged constantly. For different test runs, the channel spacing was varied, and the fracturing events were documented by a series of cameras to be described. These cameras yield information such as crack paths (i.e., by the on-board camera) and floe size distributions (i.e., by the helicopter camera).

Post-print version of the paper by Lu et al.
in Int J Cold Region of Science and Technology, 156 (2018) 102-116,
https://doi.org/10.1016/j.coldregions.2018.07.011

At the same time, ship data such as ship's position, inertia, propulsion and wind data were also continuously stored with conventional instruments. These data are utilised to back calculate the global ice force encountered by the icebreaker during the tests. Detailed instrumentation information along with the adopted method are presented in Section 4.2.

3.2 On-board Camera

Among all the installed camera systems, a specific 'parallel channel camera' at the port side of Oden (see Fig. 2) was employed to visually document the fracturing events during the tests. The camera is Pan-Tilt-Zoom (PTZ) enabled, meaning that we can remotely control its pan, tilt angle and in/out zoom. A consistent recording frequency of 1 fps was used throughout the duration of the test. Note here that we are not studying the crack propagation process in great detail; it is only the crack occurrence frequency, propagation length and directions that are of interest. Therefore, a higher image rate is not needed to track the details of each crack.

After a careful selection of camera parameters and considerations regarding installation locations, we managed to remotely adjust the camera before each test to capture both the neighbouring channel (from 30~300 m apart) and a part of the ship's bow as a reference (see the coverage in Fig. 3). Additionally, important parameters, such as camera viewing angle and tilt angle, are available as outputs for each image. This enables us to quantify each individual crack's propagation distance and direction towards the neighbouring parallel channels. The schematic set-up of the on-board camera's coverage and a sample image with a channel spacing of approximately 80 m is illustrated in Fig. 3.

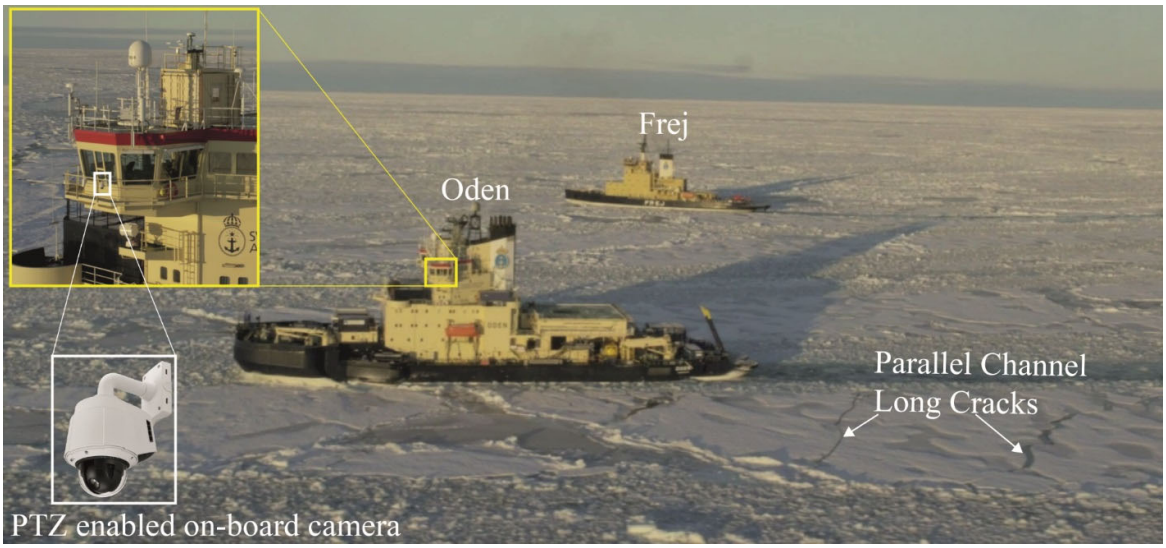

Fig. 2. On-board camera installation location and the overall test environment.

Post-print version of the paper by Lu et al.
in Int J Cold Region of Science and Technology, 156 (2018) 102-116,
https://doi.org/10.1016/j.coldregions.2018.07.011

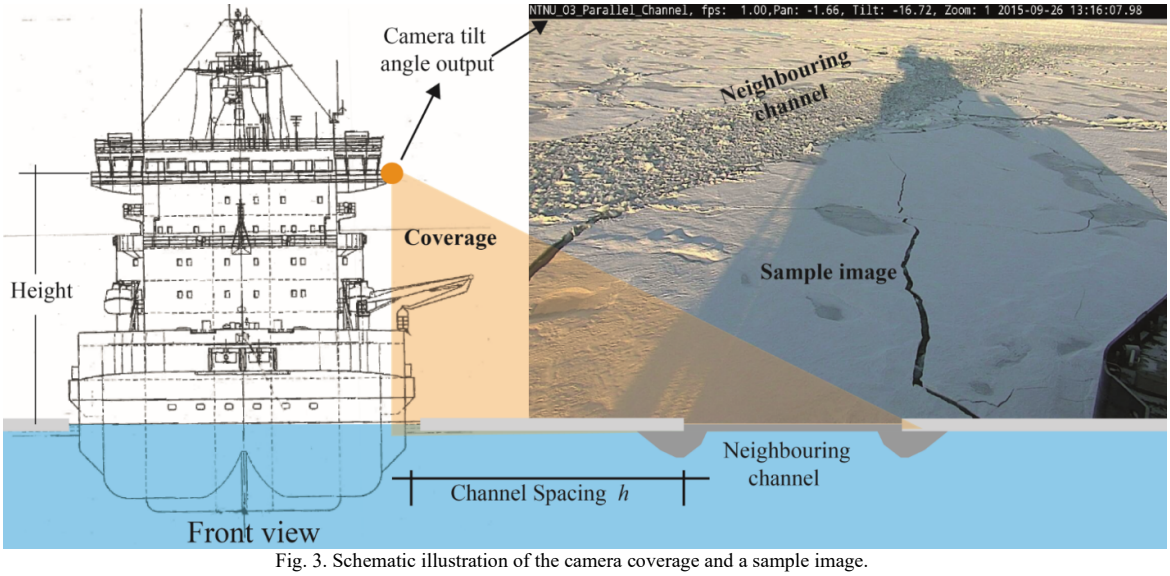

Fig. 3. Schematic illustration of the camera coverage and a sample image.

3.3 Helicopter Camera Images

During the expedition, an AS-335NP helicopter based on Oden was employed to capture images over the ice field with a camera system before and after each ice management operation. The camera system consists of a camera support (i.e., ShotOver F1, see Fig. 4a) and a Red Dragon camera with a Fujinon 25–300 mm lens. The images taken by the helicopter camera are available for one of the parallel channel tests. The parallel channel tests can also benefit from these images for evaluating the actual test track on the ice and floe size distributions in between two channels. The camera's installation location and filming conditions are illustrated in Fig. 4a, and a sample image is displayed in Fig. 4b. All the images are enriched with real-time information, such as latitude, longitude, and the camera's filming parameters (i.e., Pan, Tilt and Roll angles), which are useful for later image stitching.

Post-print version of the paper by Lu et al.
in Int J Cold Region of Science and Technology, 156 (2018) 102-116,
https://doi.org/10.1016/j.coldregions.2018.07.011

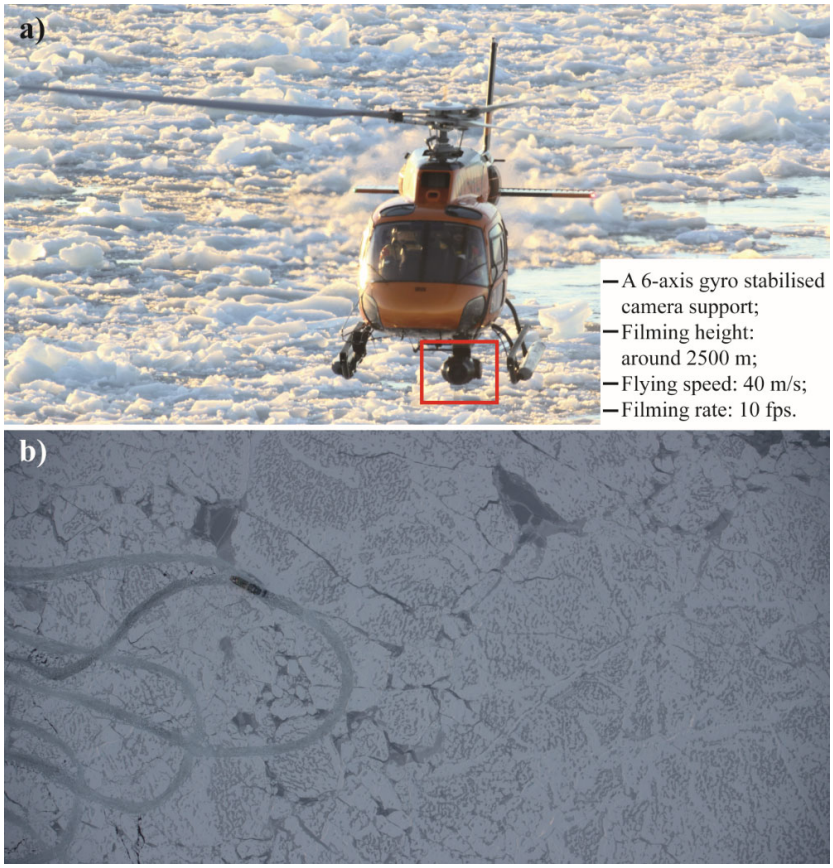

Fig. 4. Helicopter camera and a sample image.

As opposed to the on-board camera, which dynamically records the cracking events, the helicopter images, having been stitched together, can statically illustrate the overview of the test results with reasonably fine details (i.e., with discernible crack paths).

3.4 Parallel Channel Tests

We carried out three parallel channel tests during the cruise using the icebreaker Oden. These tests were usually conducted at the end of an ice management trial. The first, Test #0, lasted for only 30 minutes and was considered an initial trial. We only report the last two tests (i.e., Tests #1 and #2) in this paper.

Regarding the ice condition, a relatively more uniform ice sheet extending over a large area (or the so-called level ice) would have been ideal to validate the proposed theoretical model. However, in both of our tests, it was mainly first-year ice with melt ponds on discontinuous ice floes which are frozen together. The ice thickness is not uniform, but varies between 0.6 m to 1.5 m in the tested region. Pre-existing but refrozen or newly opened leads/cracks are also present. These discontinuous features would undoubtedly influence the occurrence and directional preference (at least locally) of the parallel channel crack. Though clouded with the presence of such inhomogeneity in the ice

Post-print version of the paper by Lu et al.
in Int J Cold Region of Science and Technology, 156 (2018) 102-116,
https://doi.org/10.1016/j.coldregions.2018.07.011

field, we are still able to identify the free boundary influences from the neighbouring channel on the fracturing events.

Test #1 was performed from 13:00 to 14:00 on September 26th, 2016. The track of Oden, with reference to the ground, is plotted in Fig. 5a. The track starts with a red colour and gradually changes to green along the plotted course. The same track, but with reference to the ice, is also highlighted in the stitched helicopter images taken immediately after the completion of Test #1 (see Fig. 5b). Compared to common ice management operations (see the tracks without colour in Fig. 5), the dedicated parallel channel tests have a relatively stricter channel spacing requirement, and the new channel is created as parallel as practically possible to the neighbouring ones. The purpose of this is to reproduce, as close as possible, the boundary conditions of the theoretical model proposed in Paper I.

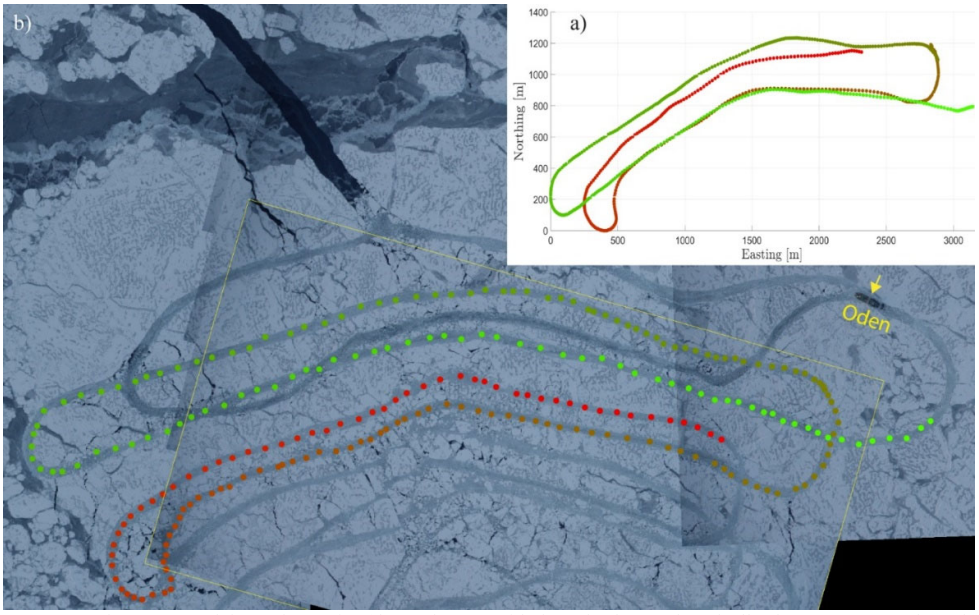

Fig. 5. Test #1: a) track over ground; b) track over ice (the track starts with the red colour and gradually changes to green along the course).

With accumulated experience, Test #2 was performed from 08:00 to 11:30 on September 29th, 2016. The initially planned track is plotted in Fig. 6a, with the intended parallel channel fracturing events exposed to Oden's portside, where the on-board camera is installed. Unfortunately, no immediate helicopter flights were arranged after the test, and therefore, no useful helicopter images are available to study the floe size distribution of Test #2. During the test, a northward ice drifting speed of approximately 0.18 m/s to 0.2 m/s was logged at 09:38. After some trial plots, by assuming a uniform ice drifting speed of 0.15 m/s northward, we managed to produce Fig. 6b as an approximate ship track over the ice. This approximated track corresponds well with the satellite image (in its original form in Fig. 7) covering the area where Test #2 was performed.

Post-print version of the paper by Lu et al.
in Int J Cold Region of Science and Technology, 156 (2018) 102-116,
https://doi.org/10.1016/j.coldregions.2018.07.011

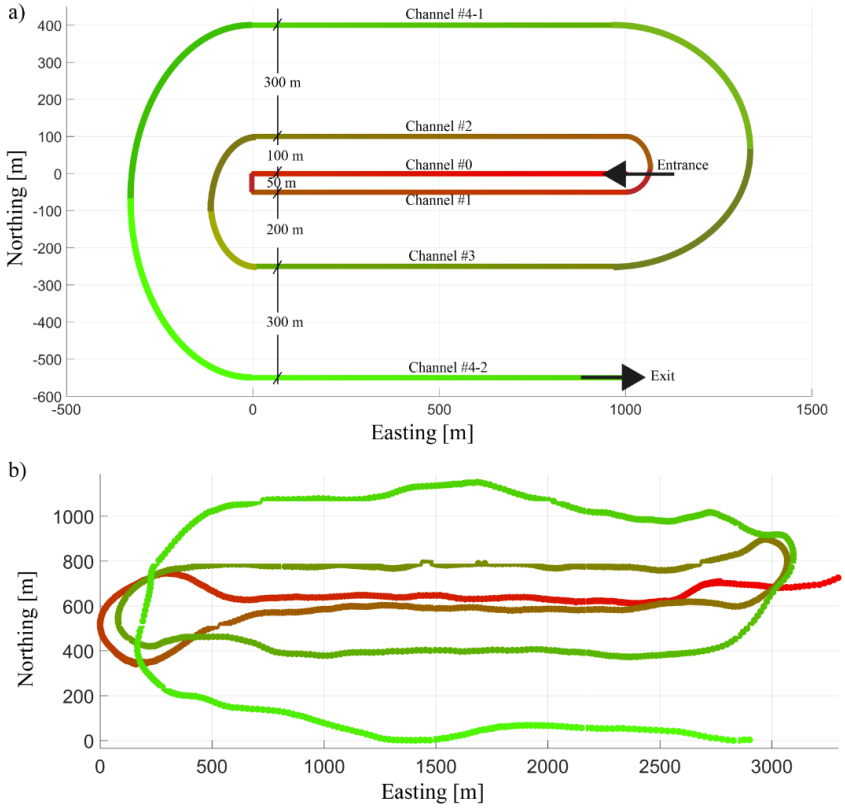

Fig. 6. Test #2: a) planned track; b) estimated ship track over ice, assuming a uniform northward ice drifting speed of 0.15 m/s.

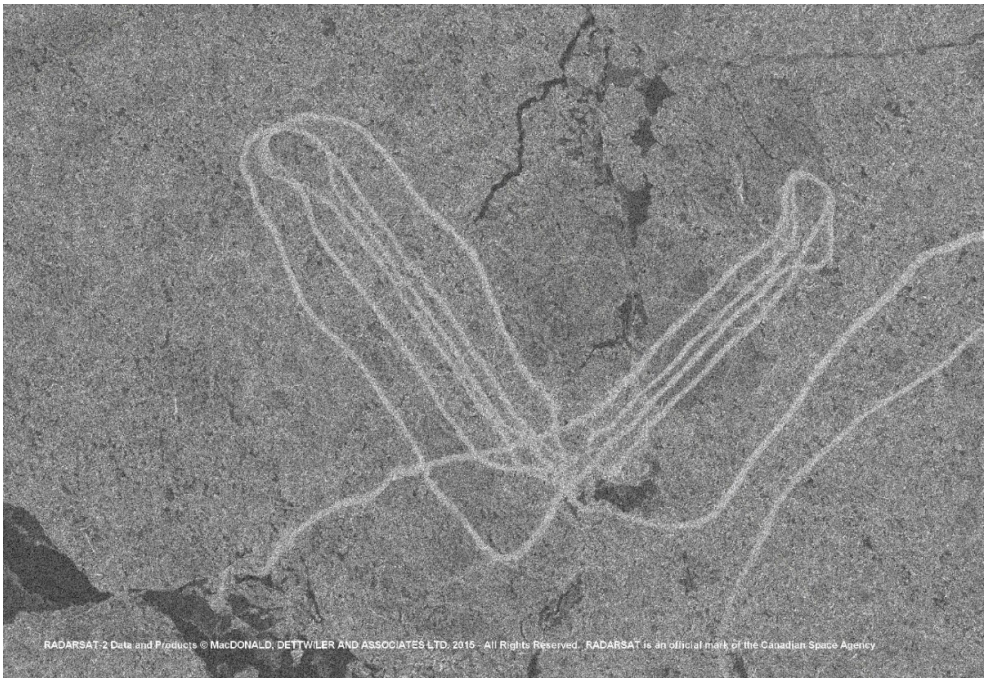

Fig. 7. Actual ship track over ice of Test #2 (the left one) with reasonable resemblance to Fig. 6b.

Post-print version of the paper by Lu et al.
in Int J Cold Region of Science and Technology, 156 (2018) 102-116,
https://doi.org/10.1016/j.coldregions.2018.07.011

4 Methods

Most of the collected data are in the form of images. Image analysis algorithms have been developed to extract values from the images, such as the floe size (L, defined in Eq. (4)), floe ratio (i.e., L/h) and crack paths (Lu et al., 2016). This paper extends the analysed results further to examine their statistical properties. Specifically, we extracted the floe size distributions from the helicopter images in Test #1. This yields information regarding the maximum floe size L_{MCD} over channel spacing h, which is used to validate the theoretical prediction in Eq. (3).

In Test #2, aside from the on-board camera dynamically recording the occurrence of long crack formations, the ship's position, inertia, propulsion, and wind data were continuously recorded. These data enable us to calculate the ice force acting on the ship and can further be converted into comparable ice fracturing force components against the theoretical predictions in Eq. (1).

4.1 Image Analysis

4.1.1 Helicopter images from Test #1

The helicopter was sent off immediately (approximately 30 min) after Test #1 to take an overall photograph of the ice management effects in the region. Information on parallel channel Test #1 can be retrieved from the relevant helicopter images (highlighted in the yellow box in Fig. 5). We choose Fig. 8 as the base image for our analysis because it covers the major part of Test #1. With the average channel spacing information labelled in the figure, we can immediately see that most of the parallel channels' fracturing events take place with spacings below 100 m. More fracturing events are found with narrower channel spacing, e.g., 30 m. As the spacing distance reaches approximately 140-200 m, few fully through ice-floe fractures can be identified.

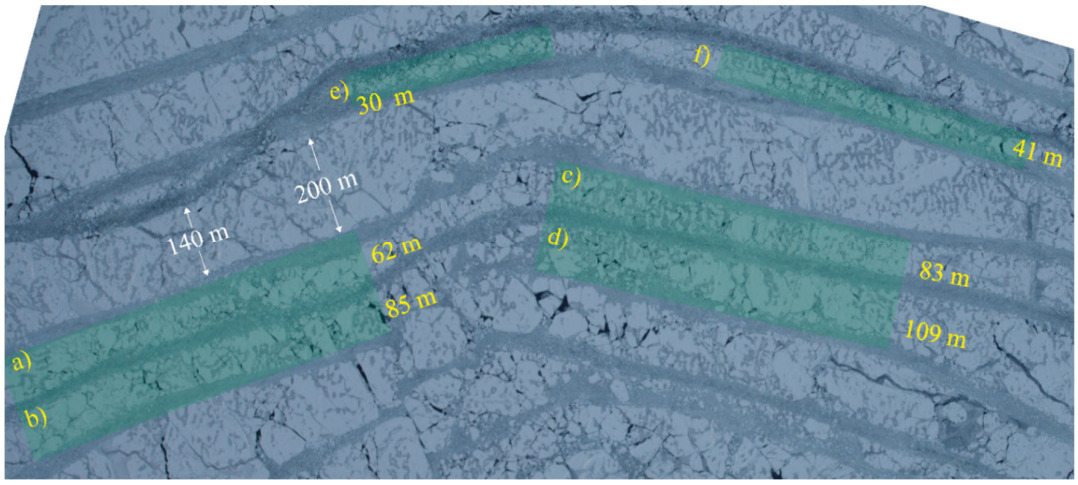

Fig. 8. Chosen regions for analysis.

Post-print version of the paper by Lu et al.
in Int J Cold Region of Science and Technology, 156 (2018) 102-116,
https://doi.org/10.1016/j.coldregions.2018.07.011

We chose six regions (shaded in green in Fig. 8) with different parallel channel spacing h values to study its influence on the fracturing events. The floe size distribution within each region is extracted for evaluation using the image processing technique described by Lu et al. (2016). The technique involves the following procedures. We first transform the original image into binary images with different grey scales to identify the border of ice floes and visually discernible cracks. The identified ice borders usually cover only a part of the perimeter of the ice floe. Then the visually discernible cracks were propagated to merge with the identified partial ice borders until a convex shaped ice floe is identified/extracted. The extracted ice floes, highlighted with yellow polygons, are illustrated in Fig. 9 for the selected regions.

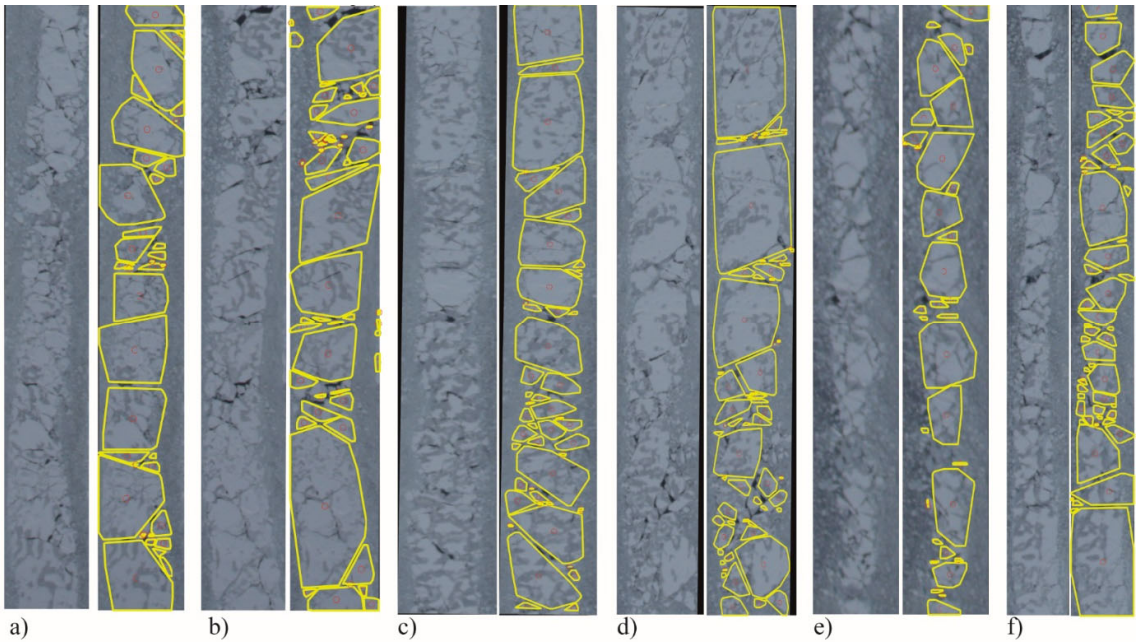

Fig. 9. Ice floe extraction based on propagating seeding cracks: a)~f) represent the different regions in Fig. 7.

To put the visual results into perspective, the extracted ice floes in Fig. 9 are patched back into the original ice field in Fig. 11, which shows the potential of the previously developed algorithm to quantify the floe size distribution after an ice management operation (Lu et al., 2016).

Post-print version of the paper by Lu et al.
in Int J Cold Region of Science and Technology, 156 (2018) 102-116,
https://doi.org/10.1016/j.coldregions.2018.07.011

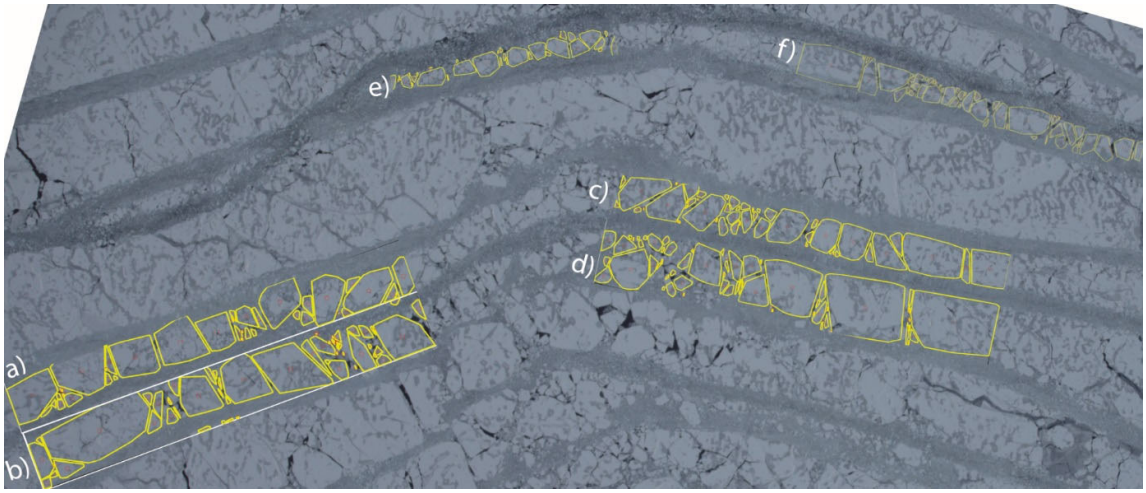

Fig. 10. Ice floe segmentation in the selected ice field.

Despite the limited test samples presented in Figs. 8 and 9, statistical analyses of the floe size distributions are conducted. Emphasis is placed on the ratio of the maximum floe size L_{MCD} over its channel spacing h, which can theoretically be predicted by Eqs. (2) and (3). While quantifying the general floe size L (and L_{MCD}) from Fig. 9, the concept of the Mean Calliper Diameter (MCD) is used as in Eq. (4) to characterise the irregular floe size, as follows:

$$L_i = \sqrt{4A_i/\pi} \qquad i = 1,2,...,...N_{total}$$
$$L_{MCD} = \max(L_i) \tag{4}$$

A_i in Eq. (4) is the area of the individual ice floe and N_{total} is the total number of ice floes.

For the floe size distributions, different distributions in Eqs. (5) to (7) have been proposed in the ice literature (e.g., see the review by Lu et al. (2008)). The formulations are presented with parameters C_0, D, γ, L_0, and L_r, which need to be fitted given the measured floe size distributions. Particularly, L_0 and L_r correspond to the mean and maximum floe size, respectively (Lu et al., 2008). In this paper, all three types of distribution functions are utilised to fit the floe sizes in Fig. 9 with a nonlinear least square fitting method.

$$\text{Power-Law distribution:} \quad \frac{N(>L)}{N_{total}} = C_0 L^{-D} \tag{5}$$

$$\text{Upper Truncated Power-Law distribution:} \quad \frac{N(>L)}{N_{total}} = C_0 (L^{-D} - L_r^{-D}) \tag{6}$$

Post-print version of the paper by Lu et al.
in Int J Cold Region of Science and Technology, 156 (2018) 102-116,
https://doi.org/10.1016/j.coldregions.2018.07.011

238 Weibull distribution: $\frac{N(>L)}{N_{total}} = \exp[-(\frac{L}{L_0})^{\gamma}]$ (7)

239

240 **4.1.2 On-board camera images from Test #2**

241 During the test, the on-board camera captured all the long cracks emanating from the portside bow area of Oden.
242 With the acquired images, it was later found that automatically tracking the occurrence of fracturing events
243 appeared to be rather challenging due to the presence of significant visual noise. Therefore, the on-board camera
244 images were processed manually in a rather straightforward manner. We reviewed all the recorded images and
245 identified all the occurrences of long cracks. In each of the events, we highlighted the far side parallel channel and
246 the corresponding visible crack. Afterwards, these images were rectified following a procedure described and
247 applied in other relevant Arctic marine operations (Lu and Li, 2010, Zhang et al., 2012a, Zhang et al., 2012b).

Post-print version of the paper by Lu et al.
in Int J Cold Region of Science and Technology, 156 (2018) 102-116,
https://doi.org/10.1016/j.coldregions.2018.07.011

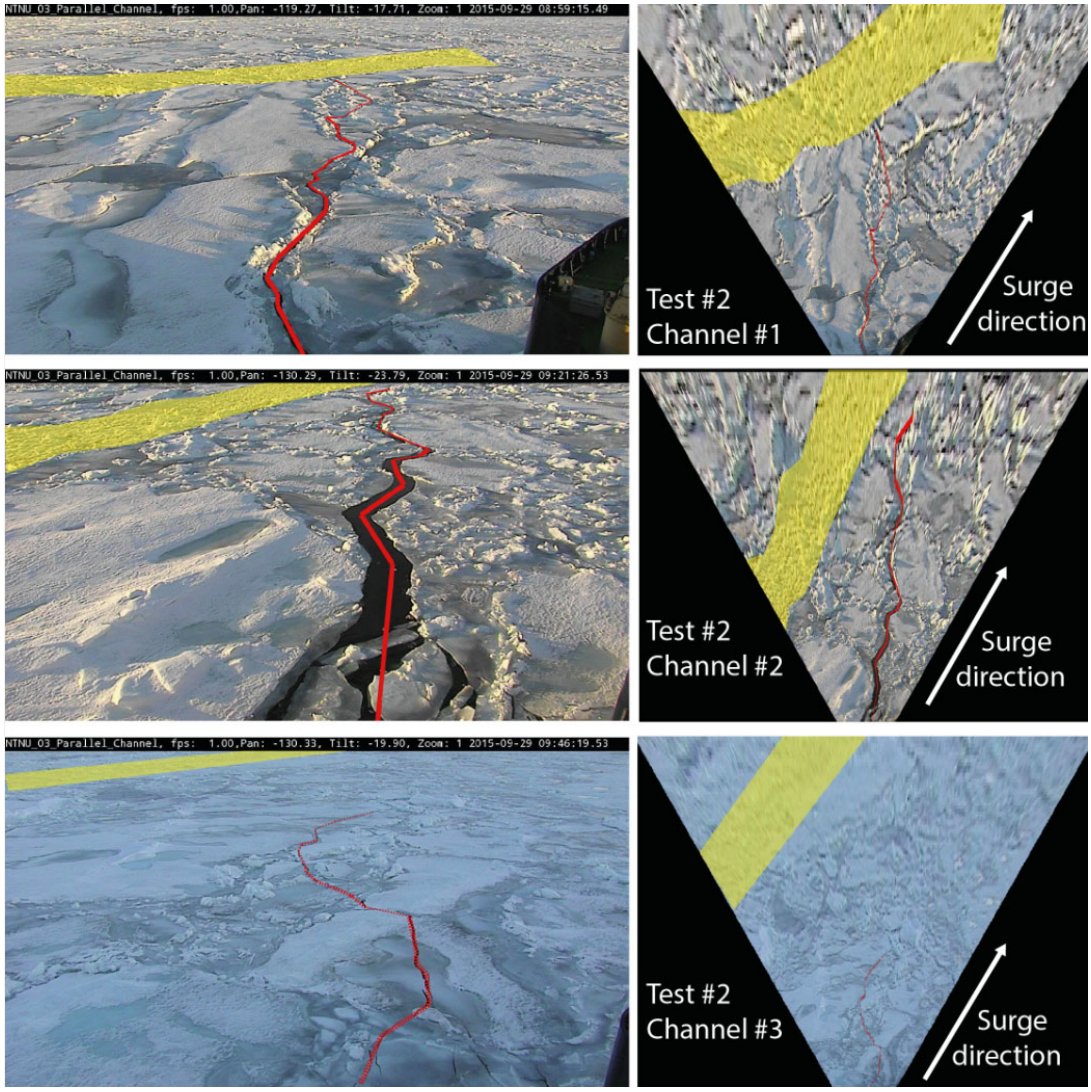

Fig. 11. Fracturing events captured by the on-board camera with different channel spacing, left: original highlighted images; right: rectified images.

Fig. 11 shows three sampled fracturing events with different channel spacing widths. Rows #1 to #3, respectively, correspond to tests in Channels #1 to #3 in Fig. 6. The original images are in the left column and the rectified images are in the right column. The images show that the tortuous crack propagation path is influenced locally by the weak zones within the ice field. However, the overall propagation direction of these long cracks is largely dictated by the neighbouring parallel channel when the spacing is less than approximately 200 m, i.e., they tend to propagate towards free boundaries. On the other hand, the long cracks, labelled by 'dashed lines' in Channel #3 (Row #3 in Fig. 11), are events in which the cracks did not manage to propagate fully through to the far side channel. In this scenario, the channel spacing of approximately 200 m is too far for the long crack to develop fully.

These rectified images are utilised to document the frequency of long cracks occurring, which is useful in supporting the floe size distribution analysis in Test #1.

4.2 Ice Force Estimation based on measurements

The direct measurement of the global ice force R_{ice} on an icebreaker is usually challenging. In this paper, we adopt an alternative approach to derive the ice force history R_{ice} during Test #2 by a purposely developed method (Kjerstad et al., 2018). The method is largely based on Eq. (8), in which the ship's propulsion force R_{prop}, hydrodynamic resistance R_{hydro}, and wind resistance R_{wind} are calculated with established methods and the conventional measurements on board. In particular, a state estimator algorithm was formulated to estimate the 6 Degrees of Freedom (DoFs) accelerations $\dot{V}$ of the ship to calculate the term $M\dot{V}$ (Kjerstad et al., 2018). Thereafter, the ice force history R_{ice} is derived.

$$M\dot{V} = R_{prop} + R_{hydro} + R_{wind} + R_{ice} \tag{8}$$

Fig. 12 illustrates the relevant sensors collecting the useful information for Eq. (8) and their respective installation locations. Four Inertia Measurement Units (IMUs) were installed on board Oden. The local linear accelerations and rotational velocities at the installation location were measured. Combining information from all these non-coplanar IMUs, we can retrieve rather accurate accelerations $\dot{V}$ of the ship. For the term R_{prop}, Oden is equipped with two Controlled Pitch (CP) propellers with a diameter of 4.8 m. One is installed on the port-side and the other on the starboard-side. The propellers are propelled by 4 medium speed, 8-cylinder Sulzer diesel engines. The total propulsion is 18 MW (Johansson and Liljestrom, 1989b). During Test #2, the ship propulsion P_s in [kW] is measured from the two propellers in the port and starboard sides of Oden. Such measurements can be utilised to calculate R_{prop} following the established method (Kjerstad et al., 2018).

To validate the crack driving force F_X and/or F_Y in Eq. (1), R_{ice} is calculated according to Eq. (8) with other known terms. However, R_{ice} is further composed of many other terms involving different ice-structure physical interaction processes, e.g., ice crushing at the contact area, ice fracturing, and submerging and sliding of ice blocks along the ship body. The component of interest to our validation is the ice fracturing component R_f, and we propose a method to quantify it. This is achieved by utilising a modified Lindqvist formulation (Lindqvist, 1989) for ice resistance in the current test condition.

Post-print version of the paper by Lu et al.
in Int J Cold Region of Science and Technology, 156 (2018) 102-116,
https://doi.org/10.1016/j.coldregions.2018.07.011

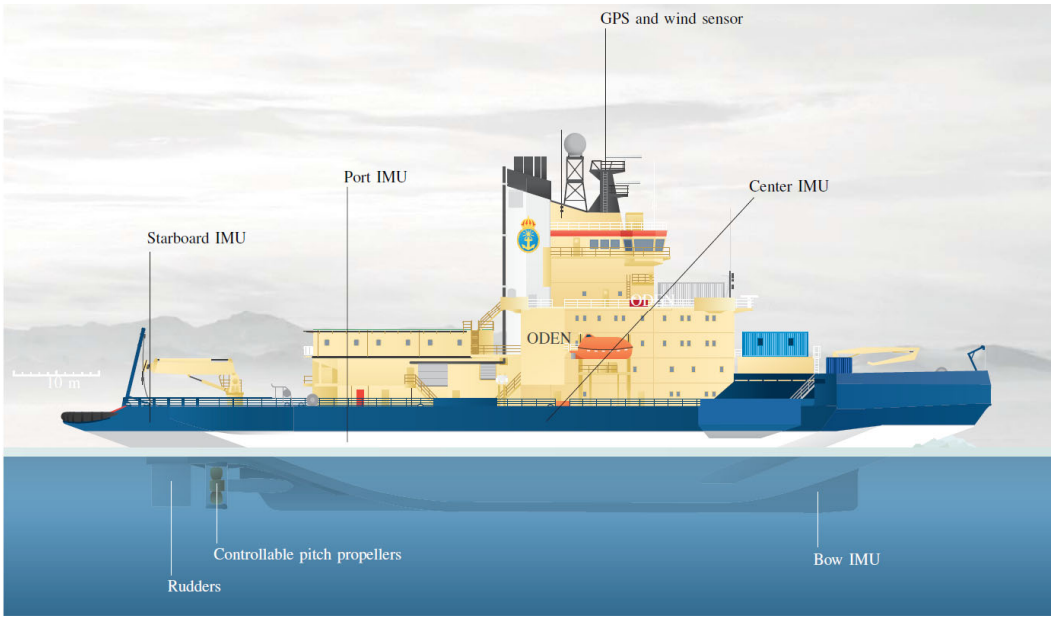

Fig. 12. Relevant sensors and their respective installation locations (originally from Kjerstad et al. (2018)).

4.2.1 From ice force R_{ice} to its ice fracturing component R_f

First, for the ship-level ice interaction process (e.g., see Section 2.1 in Paper I), the level ice resistance R_{ice}^{Level} is formulated in Eq. (9) by Lindqvist (1989). R_{ice}^{Level} consists of the following components: the ice crushing component R_c; the ice bending component R_b; a component R_s, which involves the submerging and sliding of broken ice blocks during the ship transit; and its speed dependency component $(9.4v/\sqrt{gL_{ship}})R_s$.

$$R_{ice}^{Level} = (R_c + R_b)(1 + 1.4\frac{v}{\sqrt{gt}}) + R_s(1 + 9.4\frac{v}{\sqrt{gL_{ship}}}) \tag{9}$$

Specially, the submergence term R_s is re-written in Eq. (10), as follows:

$$\begin{aligned} R_s &= -1\cdot(\rho_w - \rho_{ice})gt(A_{s1} + \mu_{i-s}A_{s2} + \mu_{i-s}A_{s3}) \\ A_{s1} &= BT\frac{B+T}{B+2T} \\ A_{s2} &= B(0.7L_{ship} - T/\tan\phi - 0.25B/\tan\alpha) \\ A_{s3} &= BT\cos\psi\cos\phi\sqrt{1/\sin^2\phi + 1/\tan^2\alpha} \end{aligned} \tag{10}$$

in which,

ρ_w and ρ_{ice}	are the density of sea water and sea ice, respectively, in [kg/m^3];
-1	denotes that R_s acts in the opposite ' x ' axis in Fig. 1b;
L_{ship}, B, and T	are length, breadth and draft of the ship, in [m];
μ_{i-s}	is the ice-structure friction coefficient. In the current paper, it is chosen as $\mu_{i-s}=0.1$, considering Oden's low friction paint (Johansson and Liljestrom, 1989a) and the recommendation by Lindqvist (1989);
A_{s1}	is related to the potential energy generated by submerging ice floes;
A_{s2}	is the ice-covered area of the ship's flat bottom, in [m^2];
A_{s3}	is the projected area (to the water plane) of the bow area, in [m^2];
ϕ, α, and ψ	are the stem angle, waterline entrance angle, and a definition of $\tan\psi=\tan\phi/\sin\alpha$. Considering Oden's bow form, in the current paper's calculation, we utilised $\phi=15^o$ and $\alpha=90^o$.

Eq. (9) is semi-empirical formula based on several assumptions and field data fitting. Its major contributor is the submergence term in Eq. (10). One of the important assumptions of R_s is that 70% of the ship's bottom area is covered with broken ice blocks. Despite Eqs. (9) and (10)'s typical use as engineering tools for the estimation of level-ice resistance as pointed out by Lindqvist (1989), the formula (or a part of the formula, especially the submergence component in Eq. (10)) is widely used for the calculation of level ice resistance in support of or for validation of more advanced model developments (e.g., (Aksnes, 2010, Lubbad and Løset, 2011, Su et al., 2010, Valanto, 2001).

Next, for the ice resistance R_{ice} during the ship–ice interactions with the presence of a nearby free channel, we argue that similar interaction processes are taking place, with some exceptions, regarding the weight of different force components (a detailed interaction process is presented in Paper I). In this paper, the ice resistance R_{ice} during a parallel channel test is assumed to be composed of the following: 1) a component R_f involving the fracture of ice dominated by forming long cracks propagating towards the nearby channel; and 2) a new submergence term, $R_s^{'}=R_s(\xi B)$, with reduced submergence area and coverage of broken ice floes beneath the icebreaker. R_{ice} is expressed in Eq. (11), as follows:

Post-print version of the paper by Lu et al.
in Int J Cold Region of Science and Technology, 156 (2018) 102-116,
https://doi.org/10.1016/j.coldregions.2018.07.011

$$R_{ice} = R_f + R_s^{'}(1+9.4\frac{v}{\sqrt{gL_{ship}}}) \quad (11)$$

in which the calculation of $R_s^{'}$ is the same as in Eq. (10) except that the ship's breadth B is reduced into ξB, with $0 \le \xi \le 1$ denoting a reduced coverage of broken ice blocks under the ship. This is a reasonable assumption considering the fact that a majority of the ice was fractured and pushed sideways due to the presence of the neighbouring parallel channel. This differs from the scenario of ship-level ice interactions in which dominant bending failure modes push broken ice blocks downward, forming a larger coverage area beneath the ship (e.g., 70%, as assumed in Eq. (10)). In the current experiment, however, we have no means to directly measure either the actual broken ice block coverage or the submergence term. Therefore, the coefficient ξ is kept open as a degree of uncertainty in the forthcoming analysis.

Based on the above derivations, we thus established the relationship between the component R_f, pertaining to sea ice fracturing during parallel channel tests, and the measurements of the ship's inertia, propulsion, hydrodynamic and wind resistance, which was further converted to the net trust R_{ice}, based on Eq. (8). An explicit form of this is written in Eq. (12).

$$R_f = M\dot{V} - R_{prop} - R_{hydro} - R_{wind} - R_s^{'}(1+9.4\frac{v}{\sqrt{gL_{ship}}}) \quad (12)$$

4.2.2 Relationship between F_X and F_Y

With Fig. 1b, we see that $|R_f| = |F_X|$ and both act at the ship bow with equal magnitude but in opposite directions. However, in Eq. (1), which is to be validated, the relationship between F_X and F_Y (i.e., β_{YX}) also needs to be identified. Therefore, the relationship between F_Y and F_X (or R_f) should be established. This is achieved by considering Oden's bow geometry. We assumed that the normal directions around Oden's bow region at the water line are evenly distributed. This is illustrated in Fig. 13, with red arrows signifying the normal directions. Fig. 13b shows that it is mainly the bow region closer to the reamer of Oden that contributes the force component in the F_Y direction; whereas it is primarily the stem region that contributes to forces in the F_X direction. Nevertheless, all the normal vectors in the ship's bow region are projected to the F_X and F_Y directions. The relationship in Eq. (13) is thus established.

Post-print version of the paper by Lu et al.
in Int J Cold Region of Science and Technology, 156 (2018) 102-116,
https://doi.org/10.1016/j.coldregions.2018.07.011

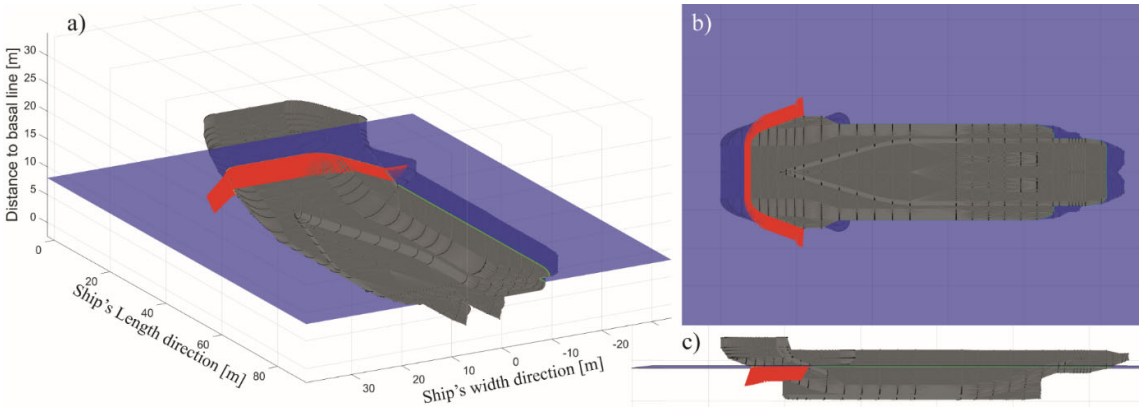

Fig. 13. Vectors (in red arrows) normal to ship bow, a) perspective view; b) view from the bottom; c) side view.

$$F_Y = \beta_{YX} F_X = -\beta_{YX} R_f \qquad (13)$$
$$\beta_{YX} = 0.6945$$

5 Results

5.1 Floe Size Distributions in Test #1

One of the important measurements during the test is the channel spacing h. From Fig. 8, we extracted the channel spacing h values for Test #1. Within the selected regions, from west to east, the varying channel spacing h and its average h_{mean} are plotted in Fig. 14. The averaged channel spacing h_{mean} shall be utilised to normalise the floe size L in the following results presentations. Without further differentiation, h_{mean} is from here on written as h for convenience and also for comparison purposes with results from Test #2.

Post-print version of the paper by Lu et al.
in Int J Cold Region of Science and Technology, 156 (2018) 102-116,
https://doi.org/10.1016/j.coldregions.2018.07.011

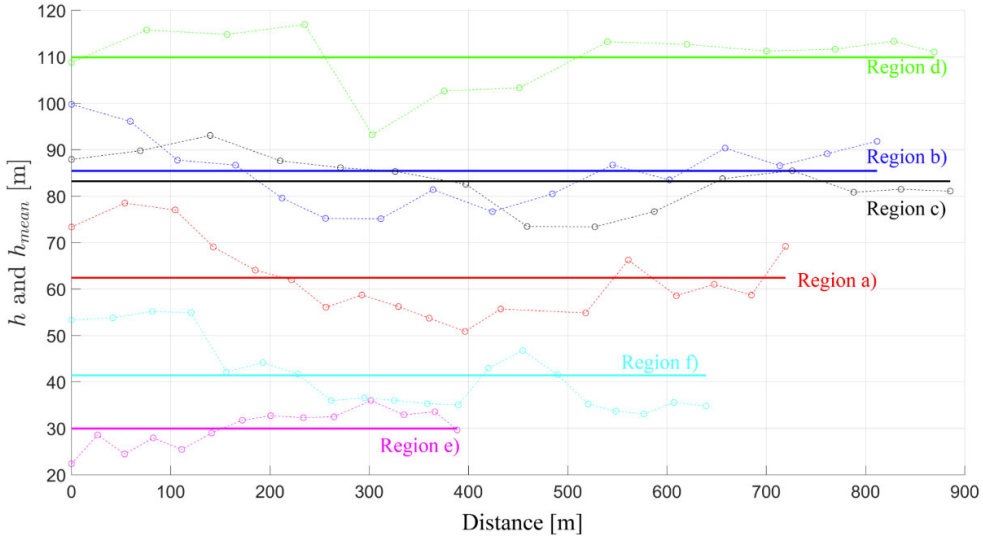

Fig. 14. Channel spacing variations for the selected regions in Test #1.

First, all the managed floe sizes L_i, i.e., the MCD defined in Eq. (4), are collected and plotted in Fig. 15, with different channel spacing h values. In addition, the theoretical prediction of L_{MCD} using Eqs. (2) and (3) are also plotted with a varying ice thickness of $t = 0.6, 1.0,$ and $1.5\,\text{m}$. The theoretical predictions show little variation with the ice thickness and overlap with each other in Fig. 15. Attention is primarily given to the measured maximum floe size, plotted as enlarged solid markers in Fig. 15. Furthermore, in Fig. 15, we also plot the often assumed floe size versus channel spacing ratio, i.e., $L_{MCD} : h = 1$, according to Hamilton et al. (2011a, 2011b), and the proposed $L_{MCD} : h = 2$ as an upper limit by Lu et al. (2016).

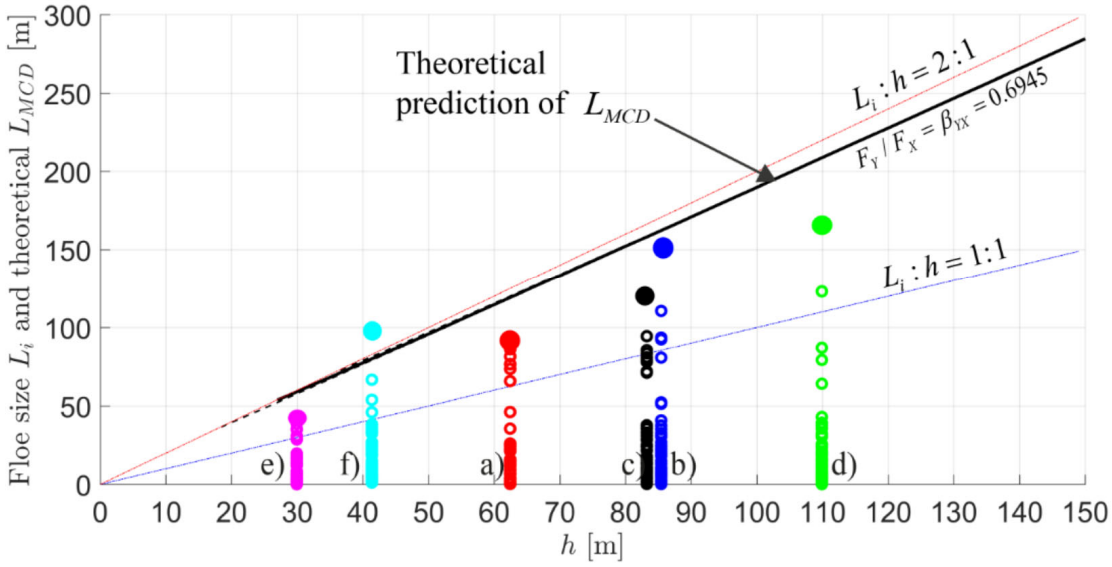

Fig. 15. Floe sizes L_i collected in Test #1 versus theoretical predictions of maximum floe size L_{MCD} given different channel spacing h values.

Post-print version of the paper by Lu et al.
in Int J Cold Region of Science and Technology, 156 (2018) 102-116,
https://doi.org/10.1016/j.coldregions.2018.07.011

In a managed ice field, in addition to the maximum floe size L_{MCD}, the overall floe size distribution is also important for ice resistance considerations. Therefore, the cumulative distribution $N(<L)/N_{total}$ of all the measured floe sizes L_i is illustrated in Fig. 16. As mentioned in Section 4.1.1, three different distribution functions were utilised to fit the measured data. An exemplified fitting for the data obtained in Channel a) by three different distribution functions is demonstrated in Fig. 17. One can see that the Weibull distribution gives a better overall fitting compared to the other two fitting methods. Similar data fitting results for other channels were also obtained.

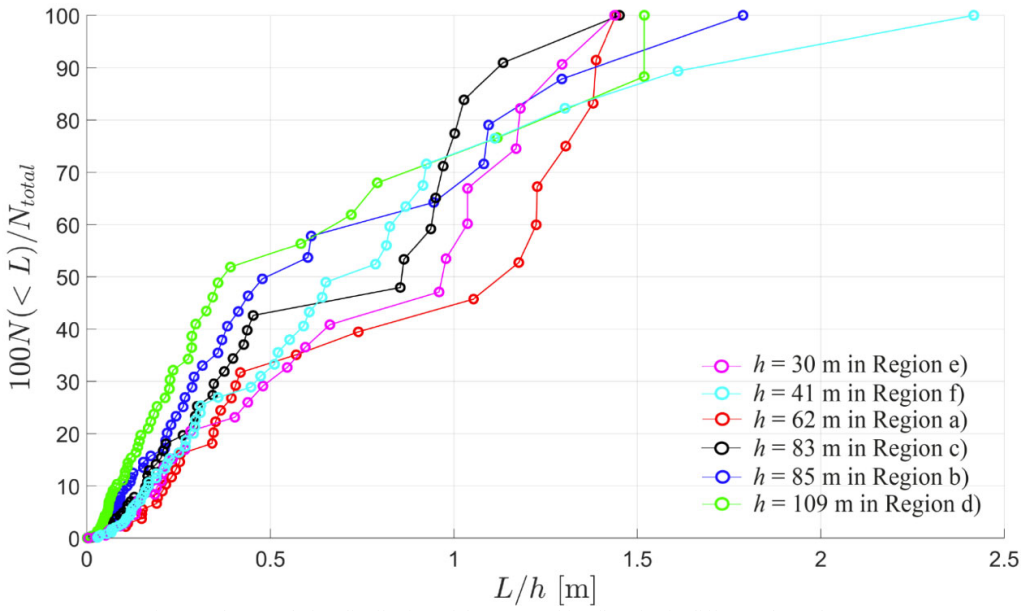

Fig. 16. The cumulative distribution of the managed ice floe size in different channels.

Post-print version of the paper by Lu et al.
in Int J Cold Region of Science and Technology, 156 (2018) 102-116,
https://doi.org/10.1016/j.coldregions.2018.07.011

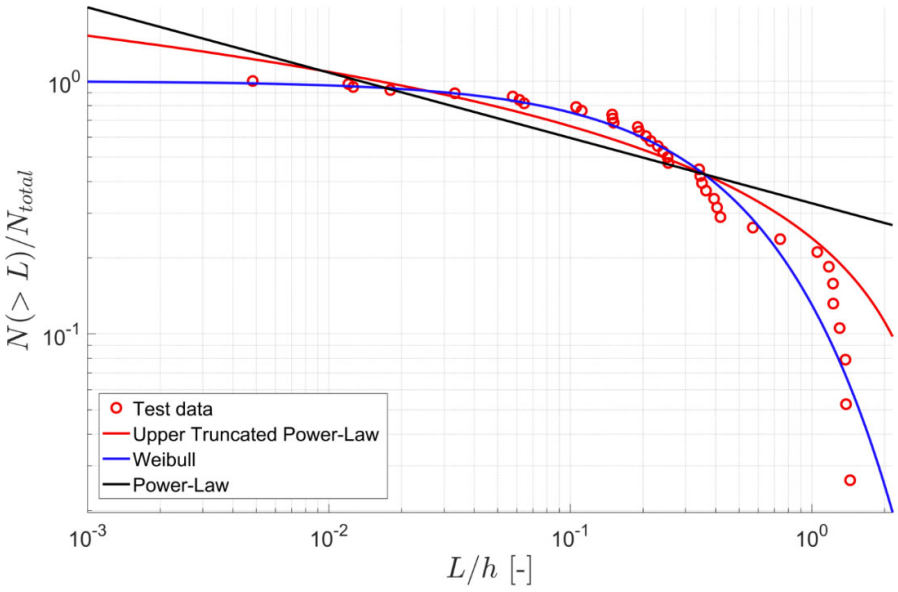

Fig. 17. Data fitting by different distribution functions for Channel a).

Given the relatively better Weibull fitting function, all the test data in the different channels are fitted accordingly in Fig. 18, along with the necessary fitting parameters γ (the shape parameter) and L_0 / L (indicating the average floe size) (Lu et al., 2008).

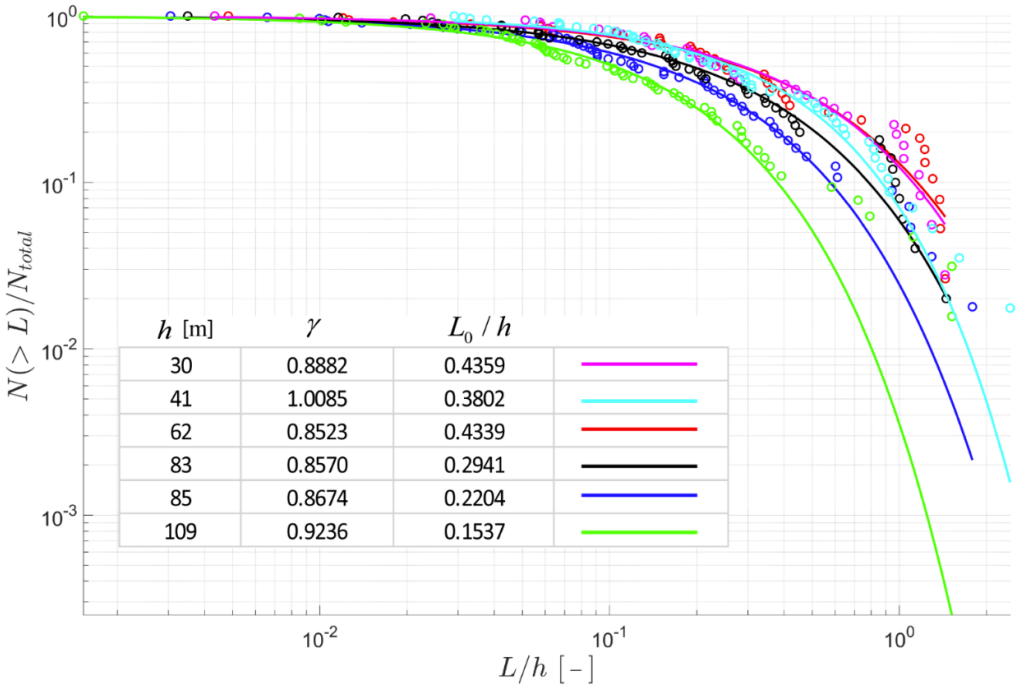

Fig. 18. Floe size distribution in Test #1 fitted by the Weibull distribution function.

Post-print version of the paper by Lu et al.
in Int J Cold Region of Science and Technology, 156 (2018) 102-116,
https://doi.org/10.1016/j.coldregions.2018.07.011

Practically, it is convenient to give an account of the floe size distribution with reference to the channel spacing h. This is summarised in Table 1.

Table 1 Channel Spacing and its influence on the floe size.

Region	h [m]	L_{MCD} [m]	$N(<h)/N_{total}$ Test	$N(<h)/N_{total}$ Weibull	$N(<1.5h)/N_{total}$ Test	$N(<1.5h)/N_{total}$ Weibull	$N(<2h)/N_{total}$ Test	$N(<2h)/N_{total}$ Weibull
e)	30	41	65%	87.65%	100%	95.01%	100%	97.91%
f)	41	100	80%	92.95%	90%	98.15%	95%	99.52%
a)	62	90	46%	86.96%	100%	94.38%	100%	97.47%
c)	83	120	77%	94.12%	100%	98.17%	100%	99.39%
b)	85	157	70%	97.56%	90%	99.49%	100%	99.89%
d)	109	163	80%	99.64%	90%	99.97%	100%	100.0%

5.2 Long Crack Formation Events in Test #2

Based on the visual analysis introduced in Section 4.1.2, the fracturing events in Test #2 were gathered and illustrated along different channels in Fig. 19. Similarly, the channel spacing h are presented in its average values. The fracture events involving the development of matured long cracks, which travelled fully through the ice reaching the nearby channel (e.g., events in the first two rows in Fig. 11), are labelled with solid markers. On the other hand, events with long cracks that did not manage to propagate fully through the ice are plotted with hollow markers.

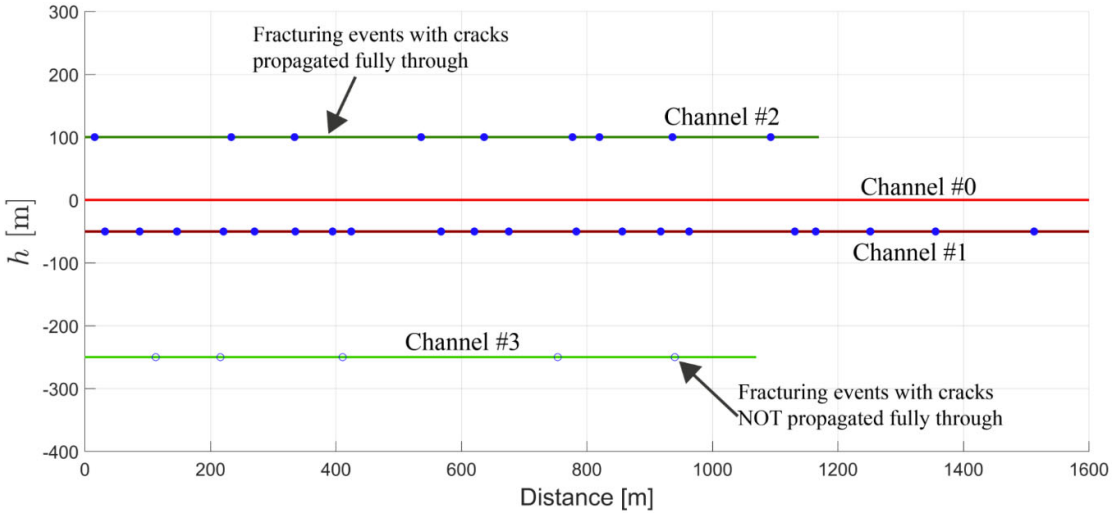

Fig. 19. Frequency of parallel channel fracturing events in Test #2 (the overall tracks are plotted in Fig. 6).

Post-print version of the paper by Lu et al.
in Int J Cold Region of Science and Technology, 156 (2018) 102-116,
https://doi.org/10.1016/j.coldregions.2018.07.011

5.3 Long Crack Propagation versus Channel Spacing in Test #2

For Test #2 on September 29th, 2016, the measured propulsion power P_s (for both the port- and starboard-sides) and velocities (calculated based on the ship's GPS data) are plotted in Fig. 20.

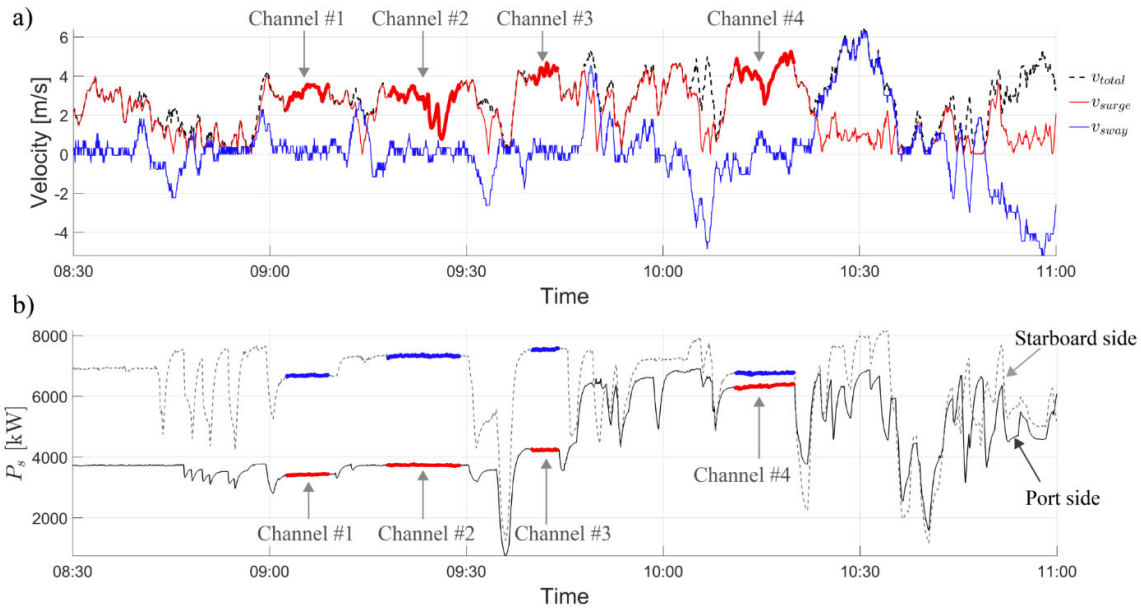

Fig. 20. Ship propulsion history and velocity data in Test #2 in different channels.

With the method developed by Kjerstad et al. (2018), based on Eq. (8) with relevant measurements, the estimated ice force history R_{ice} is presented in Fig. 21. The results within each parallel channels' test window are highlighted. Within each test window, the registered peak forces are expected to be correlated to the occurrence of long cracks observed in Fig. 19. These force peaks are averaged within each channel and are utilised to validate the theoretical prediction of F_X based on Eq. (1).

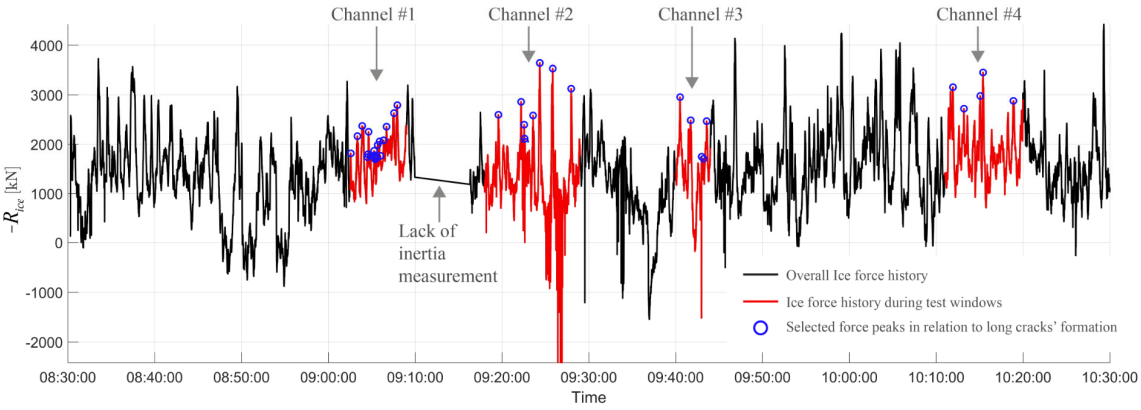

Fig. 21. Estimated ice force history based on relevant measurements in Eq. (8).

Post-print version of the paper by Lu et al.
in Int J Cold Region of Science and Technology, 156 (2018) 102-116,
https://doi.org/10.1016/j.coldregions.2018.07.011

Within Eq. (1), the channel spacing h is an important input. Based on experiences from Test #1, we logged in the measurements of h in a much more frequent and ordered manner (i.e., one record per minute). The measured channel spacing during the test is presented in Fig. 22, along with their average values.

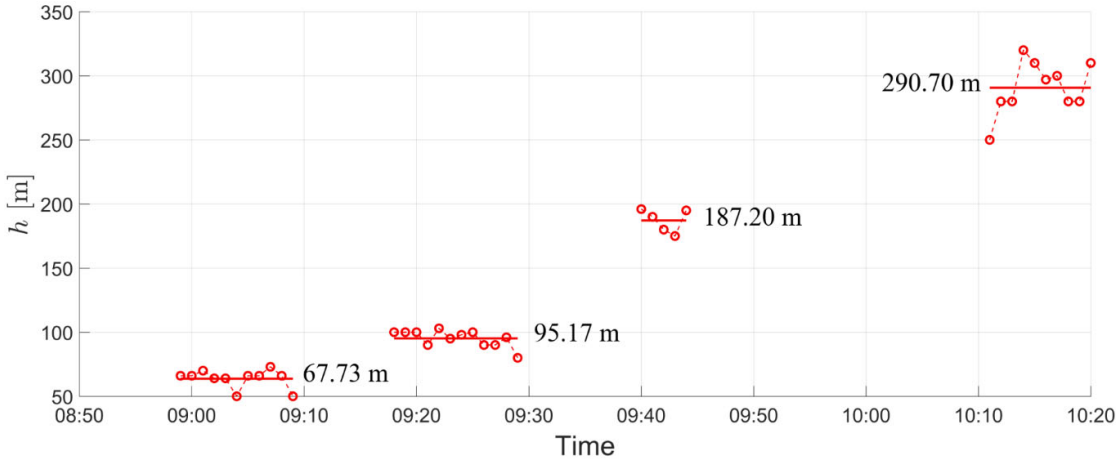

Fig. 22. Measured channel spacing with 1 min^{-1} frequency during Test #2.

In addition to h, two more input parameters (i.e., ice thickness t and fracture toughness of K_{IC}) are needed in Eq. (1). During the tests, varying ice thicknesses (0.6 m to 1.5 m) are encountered (Lu et al., 2016). Because the force peaks from Fig. 21 are utilised for comparison purpose, $t = 1.5\,\mathrm{m}$ is utilised herein to complete the calculation of F_X. For K_{IC}, because the actual fracture toughness of sea ice was not measured onsite, the calculations of F_X are based on two K_{IC} values, which can be found in the literature; i.e., $K_{IC} = 115\,\mathrm{kPa}\sqrt{\mathrm{m}}$ is based on laboratory measurements (see, e.g., (Schulson and Duval, 2009)) and $K_{IC} = 250\mathrm{kPa}\sqrt{\mathrm{m}}$ is based on field measurements (Dempsey et al., 1999). The comparison between the theoretically predicted F_X based on the proposed edge crack model and the calculated ice fracturing component R_f based on the measurements is presented in Fig. 23.

Fig. 23 presents two comparable force components, R_f and F_X, for the different channel spacing values. R_f is calculated based on Eq. (12) in Test #2 and is presented with discrete markers for Channels #1 – 4. During the calculation of R_f, the formulation of $R_s^{'}$ involves a reduction factor ξ, which was undetermined. In Fig. 23, different scenarios of ξ values are included. This means that for a measured channel spacing h, corresponding to the measured discrete value in Fig. 22, there are five markers, from the top to the bottom, sequentially represented as ξ = 0, 0.25, 0.5, 0.75 and 1.0.

Post-print version of the paper by Lu et al.
in Int J Cold Region of Science and Technology, 156 (2018) 102-116,
https://doi.org/10.1016/j.coldregions.2018.07.011

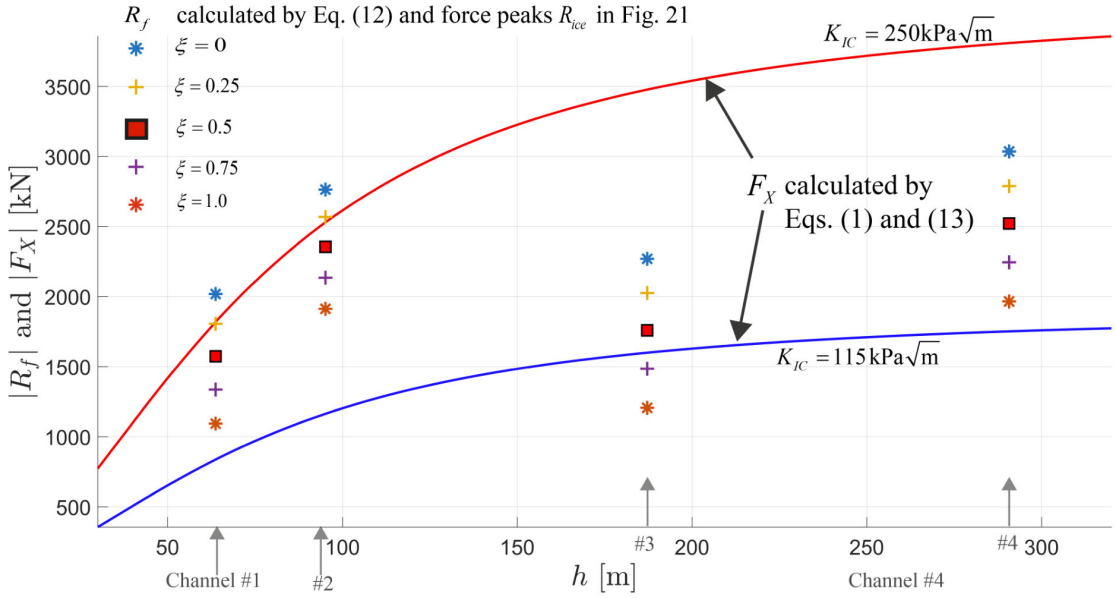

Fig. 23. Comparison between R_f, based on measured data, and F_X, based on theoretical prediction, for Test #2.

6 Discussion

6.1 Managed Ice Floe Size L_i and L_{MCD}

For Test #1, both Fig. 15 and Fig. 16 show that a significant number of small ice floes were generated in all regions regardless of the channel spacing. However, the largest ice floe, i.e., L_{MCD}, is generally increasing with channel spacing h. This is in line with the theoretical prediction plotted in Fig. 15. The enlarged solid markers in most of the regions are in close proximity to the theoretical predictions. The theoretical results appear to be only slightly influenced by the thickness variations from $t = 0.6\,\text{m}$ to 1.5 m. The theoretical predictions draw an upper bound of the maximum possible ice floe size L_{MCD}, which is supported by the current measured data in all regions (except for a slight underestimation in Region f).

In engineering practices, it is common to characterise the generated floe size with reference to the channel spacing h. Fig. 15 illustrates two common floe size approximations, i.e., $L:h=1$ according to Hamilton et al. (2011a, 2011b) and the proposed $L:h=2$ as an upper limit by Lu et al. (2016). One can see that for the approximation of L_{MCD}, the $L:h=2$ relationship appears to be a better estimation compared to its counterpart, $L:h=1$. On the other hand, the theoretical model-based formulation, i.e., Eqs. (2) and (3), takes into account the ratio of F_X and F_Y, and it can be conveniently implemented following a simple numerical recipe presented in Table 1 of Paper I. It is expected to yield more accurate results for more general engineering applications.

Post-print version of the paper by Lu et al.
in Int J Cold Region of Science and Technology, 156 (2018) 102-116,
https://doi.org/10.1016/j.coldregions.2018.07.011

For Test #2, the manually determined fracturing events in Fig. 19 also corroborate the above discussions. The fracturing events in Fig. 19 indicate the maximum possible floe sizes L_{MCD} produced between two parallel channels. We can see that most of the fracturing events occur with $1h$ or $2h$ intervals. This indicates that the produced floe sizes have possible maximum size L_{MCD} in the range of approximately $2h$.

6.2 Managed Ice Floe Size Distribution

In addition to the maximum floe size L_{MCD}, which sets an upper bound on the managed ice floe size, it is equally important to consider the floe size distributions. Fig. 16 illustrates that most of the ice floes produced are of smaller sizes than h. Among all three distribution functions, Fig. 18 shows that the Weibull distribution gives a better overall fit to the floe sizes extracted from Fig. 10. This is in accordance with the proposition of Lu et al. (2008), who argue that the Weibull distribution often gives a better fit. One disadvantage of the Weibull distribution function, however, is that large ice floes are often underestimated. This shortcoming can be overcome by the Upper Truncated Power-law distribution function, which often yields relatively conservative theoretical values in the large floe size region. Therefore, depending on one's interest, either to focus on the overall floe size distribution or to be conservative when accounting for large ice floes, different distribution functions can be chosen.

For Weibull distributions, the fitted parameters for different channels are presented in Fig. 18. For different channel spacing h values, the shape parameter γ varies little compared to the scaling parameter L_0. The general trend of L_0 / h is decreasing with increasing channel spacing values. Recalling the physical meaning of L_0 which represents the average floe size, this indicates that as the channel spacing increases, more, relatively smaller, ice floes are created. With the theoretical distribution functions and parameters at hand, the corresponding managed ice field can be numerically generated according to a similar method described by Yulmetov et al. (2014, 2016). The method first generates sufficient convex shaped ice floes of different size following the prescribed distribution. Then all the numerically generated ice floes were 'thrown' into a domain within which a 'multi-body dynamics' bases algorithm (Coutinho, 2013) is employed to resolve the overlap between ice floes. Fig. 24 demonstrates two managed ice fields with floe size distributions following the Weibull distribution and parameters in Fig. 18. To highlight the managed ice floes, brash ice within the channels is not included in Fig. 24. In practice, small rigid bodies of various shapes can be generated within the channel, reproducing the effect of brash ice (Konno et al., 2013, Konno et al., 2011, Konno, 2009). The managed ice floe size distributions demonstrated in Fig. 24 resemble the corresponding scenarios in the field in Fig. 10 b) and e). Fig. 24 also visually demonstrates that with a larger

Post-print version of the paper by Lu et al.
in Int J Cold Region of Science and Technology, 156 (2018) 102-116,
https://doi.org/10.1016/j.coldregions.2018.07.011

channel spacing, larger managed ice floes are produced, and a larger amount of comparatively smaller ice floes are also present.

In practice, for the readers' convenience, the cumulative distribution function's values for different channels are summarised in Table 1. The table demonstrates that nearly all the produced ice floe sizes are smaller than $2h$; more than 90% of the ice floe sizes are smaller than $1.5h$, and a majority (46% to 80%) of the ice floe sizes are within $1h$. With the Weibull distribution, these corresponding values are relatively higher, signifying the Weibull distribution's underestimation of large ice floes.

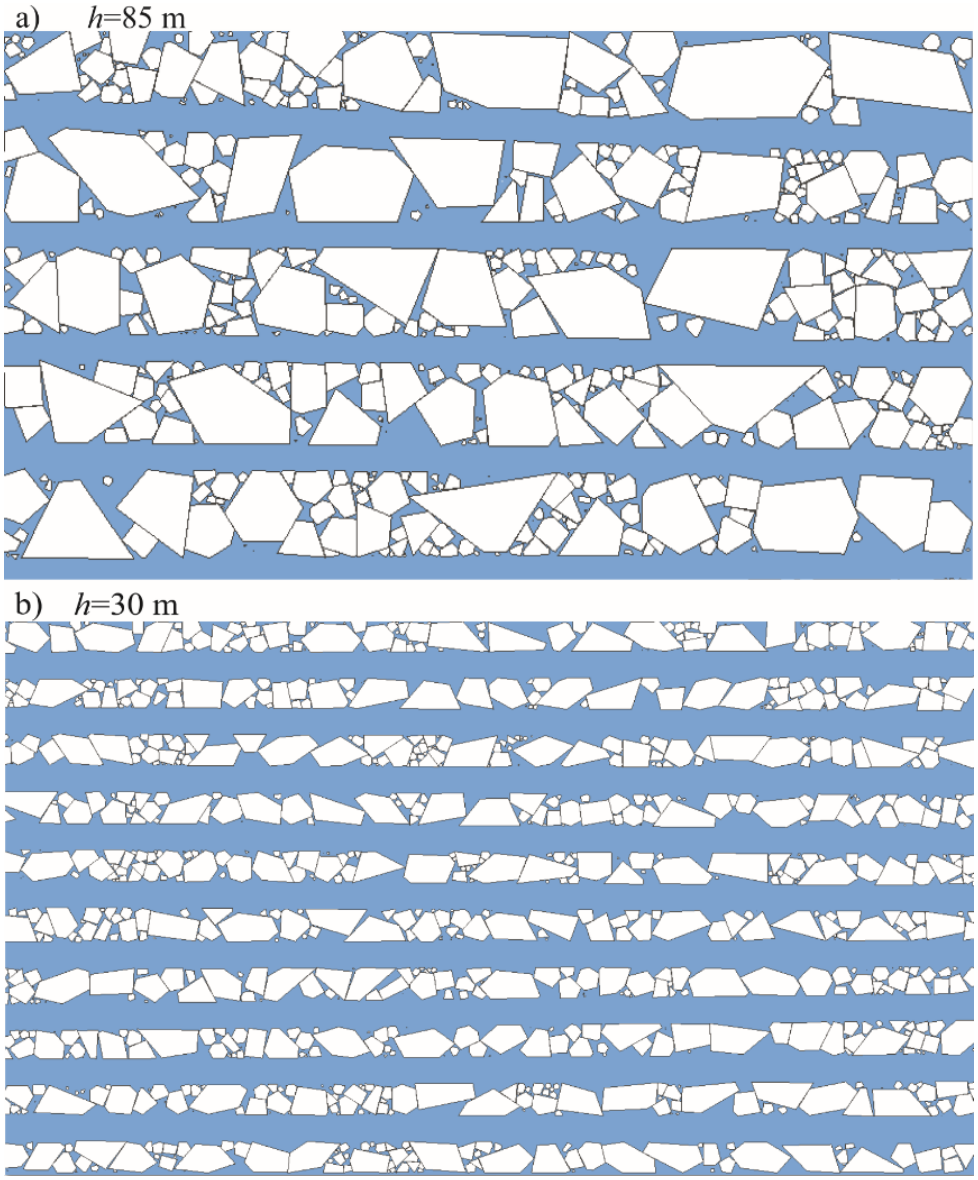

Fig. 24. Numerically generated managed ice field with different parallel channel spacing: a) channel spacing is 85 m and b) is 30 m (Note that the brash ice within the channels are not illustrated)

Post-print version of the paper by Lu et al.
in Int J Cold Region of Science and Technology, 156 (2018) 102-116,
https://doi.org/10.1016/j.coldregions.2018.07.011

6.3 Long Crack Propagation

Previous discussions primarily focus on the characterisation of managed ice fields (e.g., L_i, L_{MCD} and distribution) with a pre-condition that long cracks are already formed between parallel channels. On the other hand, the formation of long cracks is influenced by many factors, among which, the channel spacing h plays an important role. Eq. (1) formulates the minimum requirements for the propagation of a long crack. The formula was tested with the calculated R_{ice} based on field measurements in Test #2.

First, the propulsion power history during Test #2 is plotted in Fig. 20. As the channel spacing h increases, the power requirement on the port side (the side that is in close proximity to the neighbouring channel) also increases. Qualitatively, this is in line with Eq. (1), that under certain limits, a larger channel spacing leads to higher ice resistance and *vice versa*. In particular, for the case in Channel #4, the power delivery on the port- and starboard-sides becomes equivalent. This indicates that as the channel spacing increases to approximately 300 m, the parallel channels' effect becomes negligible. For more quantitative comparisons, the propulsion data is converted into the ice force R_{ice} and further into the resistance component involving ice fracture R_f with the established methods. This conversion process involves several simplifications and uncertainties, among which the largest variance lies in the reduced ice sliding component $R_s^{'} = \xi R_s$. To account for this uncertainty, the different values of $\xi = 0, 0.25$, 0.5, 0.75 and 1.0 are considered in the calculations, with the results plotted in Fig. 23. In addition, the theoretical predictions based on Eqs. (1) and (13) are plotted with the available fracture toughness values of the sea ice within the literature. Despite the scatters in Fig. 23's comparisons, we can generally see that a higher chance of favourable comparison agreement exists for the tests in Channels #1 and #2 with the results calculated by the fracture toughness of $K_{IC} = 250\,\mathrm{kPa}\sqrt{\mathrm{m}}$. This is in line with the visual observations presented in Fig. 19, in which matured long cracks are frequently formed within Channels #1 and #2 as opposed to Channels #3 and #4. This means that the primary ice failure pattern in the tests within Channels #1 and #2 are dominated by the formation of long cracks, which can be predicted by the edge crack model involving Eqs. (1) and (13), and a fracture toughness of $K_{IC} = 250\,\mathrm{kPa}\sqrt{\mathrm{m}}$.. We further consider the fact that with a narrower channel spacing h, the ice sliding component would become less significant, i.e., a smaller ξ value. In this regard, we see that a majority of R_f, calculated by a reduced ξ for Channels #1 and #2, resides well within the theoretical prediction ranges. The current quantitative comparisons made in Fig. 23, though clouded with uncertainties, show Eq. (1)'s promising potential for determining a long crack's propagation in the presence of a neighbouring parallel channel.

Post-print version of the paper by Lu et al.
in Int J Cold Region of Science and Technology, 156 (2018) 102-116,
https://doi.org/10.1016/j.coldregions.2018.07.011

6.4 Parallel Channels' Fracture Mechanisms

There are generally two ice fracturing modes during ice structure interactions, namely, the in-plane (Dempsey et al., 1993, Bhat, 1988, Bhat et al., 1991) and out-of-plane failure modes (Lu, 2014). The out-of-plane fracture's crack extension, in the form of radial cracking, is usually rather limited in length. The radial crack is bounded by a length of 2ℓ (Lu et al., 2015b, Sodhi, 1996), beyond which, local bending failure with the formation of a circumferential crack at a distance slightly larger than 1.83ℓ (Nevel, 1972, Lu et al., 2015c) shall take place. ℓ is the characteristic length defined in Eq. (1). For typical ice material floating on water, ℓ can be approximated by $\ell = 13.5t^{3/4}$ (Gold, 1971). For parallel channel spacing $h \le 2\ell \approx 30\,\mathrm{m}$, much more frequent fracture events are observed in Channel e) in Test #1, Fig. 8. Practically, the channel spacing is much larger than 2ℓ; thus, most of the observed long crack formations are essentially under the category of the in-plane failure mode, which enables a crack to propagate for a much longer distance (Lu et al., 2015a, Bhat, 1988, Bhat et al., 1991). For ships creating parallel channels in an ice field, because of the nearby free boundaries, circumferential cracks can potentially cease to take place; instead, the formed radial crack, with a maximum length of $A_0 = 2\ell$ can be further propagated, leading to the formation of long cracks. The initial location and orientation of these long cracks are difficult to characterise deterministically. In a limiting sense, in these two associated papers, we choose to analyse and validate one type of long crack, i.e., Type #1 in Figure 4 of Paper I. Based on the chosen edge crack model, a new developed formulation in Paper I enables us to determine this type of long crack's propagation and path. Consequently, the formulation yields information on the maximum channel spacing $h_{\max}$ and maximum floe size L_{MCD}. The experimental results described in this paper corroborate the theoretical prediction hitherto. However, the other failure types in Figure 4 of Paper I should not be forgotten. The joint occurrence of all these types of in-plane fracturing processes leads to the observed floe size distribution presented in this paper. The combined effect of all these fracturing processes is considered as the complete mechanism behind the observed parallel channel fracturing mechanism.

7 Conclusions

In the associated Paper I, a theoretical model was proposed to uncover the fracture mechanism for the observed long crack formations occurring between two parallel channels during ice management operations. As a continuation to the theoretical development, we reported in this paper (i.e., Paper II) two parallel channel tests performed by the icebreaker Oden during the Oden Arctic Technology Research Cruise 2015 (OATRC2015).

During the tests, we varied the channel spacing for different test runs. Within each test run, the channel spacing was maintained to the captain's best ability. In the tests, the fracturing information were collected in the form of images taken from a helicopter camera (for Test #1) and the ship's on-board camera system (for Test #2). The helicopter camera images were processed to extract the managed ice floes in Test #1 with different channel spacing h. This yields information such as the maximum ice floe size L_{MCD} and floe size distributions. In addition, major fracturing events were also documented by the on-board cameras in Test #2. The documented fracturing events indicate the maximum possible ice floes L_{MCD}. All these test results satisfactorily support the theoretical prediction in terms of L_{MCD}. Aside from the validation made upon the theoretical model, some general conclusions regarding L_{MCD} are drawn as follows:

- The size of the largest managed ice floe, L_{MCD}, within two parallel channels generally increases with the channel spacing h.
- The size L_{MCD} can be well predicted by Eqs. (2) and (3) with reasonable precision. However, for straightforward engineering applications, L_{MCD} can be approximated by twice the channel spacing, i.e., $L_{MCD} = 2h$.

In addition to the maximum managed ice floe size, we also studied the overall floe size distributions given different channel spacings h. Conclusions in this regard are drawn as follows:

- Among all three tested distribution functions, the Weibull distribution yields a comparatively better fitting to the overall floe size distributions, whereas certain underestimation exists for large ice floes;
- The Upper Truncated Power-law distribution shows a better fit to large ice floes, whereas the overall fitting is not as satisfactory as the Weibull distribution;
- A great majority of the managed ice floe sizes are smaller than the L_{MCD} values extracted in the experiment or predicted by theories;
- For Test #1, all (100%) of the managed ice floe sizes are 2 times smaller than the spacing (i.e., $< 2h$); 90% of them are smaller than 1.5 times the spacing (i.e., $< 1.5h$); and a majority of them (around 46% to 80% depending on the channel spacing) are smaller than the spacing (i.e., $< h$). The fitted Weibull distribution functions give relatively higher percentage values due to its underestimation regarding the existence of large ice floes;

- The fitted distribution function, e.g., Weibull distribution function, can be utilised to numerically generate a managed ice field (exemplified in Fig. 24). This uncovered the numerical potential in simulating the ice force in different representative managed ice fields.

Moreover, we analysed the ship's inertia, propulsion history, hydrodynamic and wind force on the icebreaker Oden in Test #2. The force component pertaining to ice fractures was derived. The conversion process involves several simplifications and uncertainties. However, the calculated results based on the measurement agree favourably with the theoretical predictions (i.e., Eq. (1)), signifying its theoretical validity. Based on the comparison and discussion, the following conclusions are drawn:

- For ice fracturing scenarios dominated by the formation of long cracks between parallel channels, Eq. (1) gives reasonable predictions for the crack propagation;
- Conversely, Eq. (1) can be utilised to quantify the maximum channel spacing $h_{\max}$, beyond which long cracks of Type #1 cease to take place;

In these two associated papers, a theoretical model was proposed and validated both numerically and experimentally. The theoretical model is based on an 'edge crack model' and is a highly idealised fracture scenario of long cracks of Type #1 (see Paper I, Figure 4). The theoretical model, in a limiting sense, predicts the maximum managed ice floe size L_{MCD}, maximum channel spacing $h_{\max}$ and required force combination (F_X and F_Y) for long crack propagation. However, the varying managed ice floe sizes produced between two parallel channels are the joint effect of several types of fracturing processes. These different types of fracturing processes (see Paper I, Figure 4) share the similarities in the sense that 1) they are under the category of in-plane splitting failure; and 2) they are influenced by a nearby free boundary. The joint effect is considered as the observed parallel channel fracturing mechanism.

Acknowledgement

The Oden Arctic Technology Research Cruise 2015 (OATRC2015) was supported by ExxonMobil Upstream Research Company and performed by the Norwegian University of Science and Technology (NTNU) in cooperation with the Swedish Polar Research Secretariat (SPRS) and the Swedish Maritime Administration (SMA).

Post-print version of the paper by Lu et al.
in Int J Cold Region of Science and Technology, 156 (2018) 102-116,
https://doi.org/10.1016/j.coldregions.2018.07.011

References

AKSNES, V. 2010. A simplified interaction model for moored ships in level ice. *Cold Regions Science and Technology,* 63**,** 29-39.

BHAT, S. U. 1988. Analysis for splitting of ice floes during summer impact. *Cold Regions Science and Technology,* 15**,** 53-63.

BHAT, S. U., CHOI, S. K., WIERZBICKI, T. & KARR, D. G. 1991. Failure analysis of impacting ice floes. *Journal of Offshore Mechanics and Arctic Engineering,* 113**,** 171.

COUTINHO, M. G. 2013. *Guide to Dynamic Simulations of Rigid Bodies and Particle Systems*, Springer.

DEMPSEY, J. P., ADAMSON, R. M. & MULMULE, S. V. 1999. Scale effects on the in-situ tensile strength and fracture of ice. Part II: First-year sea ice at Resolute, NWT. *International journal of fracture,* 95**,** 347-366.

DEMPSEY, J. P., DEFRANCO, S. J., BLANCHET, D. & PRODANOVIC, A. Splitting of ice floes. 1st International Conference: Development of Russian Arctic Offshore (RAO'93), 1993.

FARID, F., SCIBILIA, F., LUBBAD, R. & LØSET, S. 2014. Sea Ice Management Trials during Oden Arctic Technology Research Cruise 2013 Offshore North East Greenland. *22nd IAHR International Symposium on Ice.* Singapore.

GOLD, L. W. 1971. Use of ice covers for transportation. *Canadian Geotechnical Journal,* 8**,** 170-181.

HAMILTON, J., HOLUB, C., BLUNT, J., MITCHELL, D. & KOKKINIS, T. Ice Management for Support of Arctic Floating Operations. OTC Arctic Technology Conference, 2011a.

HAMILTON, J., HOLUB, C. J. & BLUNT, J. 2011b. Simulation of ice management fleet operations using two decades of Beaufort Sea ice drift and thickness time histories. *Proceedings of International Society of Offshore and Polar Engineers (ISOPE), Maui, Hawaii.*

HAMILTON, J., KOKKINIS, T., HOLUB, C., MATSKEVITCH, D., CHENG, T., HARRIS, M. & SHAFROVA, S. Near-Field Ice Management Tactics for Floating Drilling in Arctic Pack Ice. Arctic Technology Conference, 2016. Offshore Technology Conference.

JOHANSSON, B. & LILJESTROM, G. 1989a. ODEN-A STATE-OF-THE-ART ICEBREAKER. *POAC 89.*

JOHANSSON, B. & LILJESTROM, G. 1989b. Oden-icebreaker technology for the year 2000. *Transactions-Society of Naval Architects and Marine Engineers,* 97**,** 53-83.

KJERSTAD, Ø. K., LU, W., SKJETNE, R. & LØSET, S. 2018. A method for real-time estimation of full-scale global ice loads on floating structures. *Cold Regions Science and Technology*.

KONNO, A. 2009. Resistance Evaluation of Ship Navigation in Brash Ice Channels. *Proceedings of the 20th International Conference on Port and Ocean Engineering under Arctic Conditions.* Luleå, Sweden.

KONNO, A., NAKANE, A. & KNAMORI, S. 2013. Validation of Numerical Estimation of Brash Ice Channel Resistance with Model Test *Proceedings of the 22nd International Conference on Port and Ocean Engineering under Arctic Conditions.* Espoo, Finland.

KONNO, A., SAITOH, O. & WATANABE, Y. 2011. Numerical Investigation of Effect of Channel Condition against Ship Resistance in Brash Ice Channels. *Proceedings of the 21st International Conference on Port and Ocean Engineering under Arctic Conditions.* Montréal, Canada.

LINDQVIST, G. A straightforward method for calculation of ice resistance of ships. Proceedings of POAC 1989, 1989. 722-735.

LU, P. & LI, Z. 2010. A Method of Obtaining Ice Concentration and Floe Size From Shipboard Oblique Sea Ice Images. *Geoscience and Remote Sensing, IEEE Transactions on,* 48**,** 2771-2780.

LU, P., LI, Z. J., ZHANG, Z. H. & DONG, X. L. 2008. Aerial observations of floe size distribution in the marginal ice zone of summer Prydz Bay. *Journal of Geophysical Research: Oceans,* 113**,** n/a-n/a.

LU, W. 2014. *Floe Ice - Sloping Structure Interactions.* Doctor of Philosophy Doctoral, Norwegian University of Science and Technology.

LU, W., LUBBAD, R. & LØSET, S. 2015a. In-plane fracture of an ice floe: A theoretical study on the splitting failure mode. *Cold Regions Science and Technology,* 110**,** 77-101.

LU, W., LUBBAD, R. & LØSET, S. 2015b. Out-of-plane failure of an ice floe: Radial-crack-initiation-controlled fracture. *Cold Regions Science and Technology,* 119**,** 183-203.

LU, W., LUBBAD, R., LØSET, S. & KASHAFUTDINOV, M. 2015c. Fracture of an ice floe: Local out-of-plane flexural failures versus global in-plane splitting failure. *Cold Regions Science and Technology*.

LU, W., LUBBAD, R., LØSET, S. & SKJETNE, R. 2016. Parallel Channel Tests during Ice Management Operations in the Arctic Ocean. *Arctic Technology Conference 2016.* St. John's, Newfoundland and Labrador.

LUBBAD, R. & LØSET, S. 2011. A numerical model for real-time simulation of ship-ice interaction. *Cold Regions Science and Technology,* 65**,** 111-127.

644 LUBBAD, R., LØSET, S., HEDMAN, U., HOLUB, C. & MATSKEVITCH, D. 2016. Oden Arctic Technology
645 Research Cruise 2015. *Proc. of the Arctic Technology Conference (ATC).* St. Johns's, Newfoundland
646 and Labardor, Canada.
647 LUBBAD, R., LØSET, S. & LU, W. 2012. Oden Arctic Technology Research Cruise 2012: Data report Part I,
648 SAMCoT report. Trondheim: Norwegian University of Science and Technology.
649 LUBBAD, R., LØSET, S. & LU, W. 2013. Oden Arctic Technology Research Cruise 2013: Field-Data report.
650 Trondheim: Norwegian University of Science and Technology.
651 MATSKEVITCH, D., LØSET, S., SHAFROVA, S., MITCHEL, D. & HOLUB, C. Application of Satellite
652 Remote Sensing Data during OATRC 2015 Research Expedition. Arctic Technology Conference,
653 2016. Offshore Technology Conference.
654 NEVEL, D. E. The ultimate failure of a floating ice sheet. International Association for Hydraulic Research, Ice
655 Symposium, 1972. 17-22.
656 SCHULSON, E. M. & DUVAL, P. 2009. *Creep and fracture of ice,* Cambridge, Cambridge University Press.
657 SHAFROVA, S., HOLUB, C., HARRIS, M., CHENG, T., MATSKEVITCH, D., FOLTZ, R. & MITCHELL, D.
658 Common Operational Picture COP Requirements for Floating Drilling in Pack Ice. Arctic Technology
659 Conference, 2016. Offshore Technology Conference.
660 SODHI, D. S. Deflection Analysis of Radially Cracked Floating Ice Sheets. OMAE, 1996. 97-102.
661 SU, B., RISKA, K. & MOAN, T. 2010. A numerical method for the prediction of ship performance in level ice.
662 *Cold Regions Science and Technology,* 60**,** 177-188.
663 VALANTO, P. 2001. The resistance of ships in level ice. *SNAME,* 109**,** 53-83.
664 YULMETOV, R., LØSET, S. & LUBBAD, R. 2014. An Effective Numerical Method for Generation of Broken
665 Ice Fields, Consisting of a Large Number of Polygon-Shaped Distinct Floes. *Proceedings of the 22nd*
666 *IAHR International Symposium on Ice.* Singapore.
667 YULMETOV, R., LUBBAD, R. & LØSET, S. 2016. Planar multi-body model of iceberg free drift and towing in
668 broken ice. *Cold Regions Science and Technology,* 121**,** 154-166.
669 ZHANG, Q., SKJETNE, R., LØSET, S. & MARCHENKO, A. Digital image processing for sea ice observations
670 in support to Arctic DP operations. ASME 2012 31st International Conference on Ocean, Offshore and
671 Arctic Engineering, 2012a. American Society of Mechanical Engineers, 555-561.
672 ZHANG, Q., VAN DER WERFF, S., METRIKIN, I., LØSET, S. & SKJETNE, R. Image processing for the
673 analysis of an evolving broken-ice field in model testing. ASME 2012 31st International Conference on
674 Ocean, Offshore and Arctic Engineering, 2012b. American Society of Mechanical Engineers, 597-605.

675